



Javier Alejandro Pachas Clemente

**Search for CP Violation through the
 $D_s^+ \rightarrow K^- K^+ K^+$ decay in the LHCb Experiment**

DISSERTAÇÃO DE MESTRADO

Dissertation presented to the Programa de Pós-Graduação em Física of the Departamento de Física, PUC-Rio as partial fulfillment of the requirements for the degree of Mestre em Física.

Advisor: Profa. Carla Göbel Burlamaqui de Mello

Rio de Janeiro
August 2015



Javier Alejandro Pachas Clemente

**Search for CP Violation through the $Ds^+ \rightarrow K^- K^+ K^+$ decay
in the LHCb Experiment**

Dissertação presented to the Programa de Pós-Graduação em Física of the Departamento de Física do Centro Técnico Científico da PUC-Rio, as partial fulfillment of the requirements for the degree of Mestre.

Profa. Carla Göbel Burlamaqui de Mello
Advisor
Departamento de Física – PUC-Rio

Prof. Arthur Marques Moraes
CBPF

Prof. Juan Martin Otálora Goicochea
UFRJ

Prof. José Eugenio Leal
Coordinator of the Centro Técnico Científico da PUC-Rio

Rio de Janeiro, August 31st, 2015.

All rights reserved.

Javier Alejandro Pachas Clemente

The author graduated in Physics from the Universidad Nacional de Ingeniería, Lima –Perú. He obtained the degree of Bachelor in 2009.

Bibliographic data

Pachas Clemente, Javier Alejandro

Search for CP Violation through the $D_s^+ \rightarrow K^- K^+ K^+$ decay in the LHCb Experiment / Javier Alejandro Pachas Clemente; advisor: Carla Göbel Burlamaqui de Mello. — 2015.

85f. : il.; 30 cm

Dissertação (Mestrado em Física) - Pontifícia Universidade Católica do Rio de Janeiro, Rio de Janeiro, 2015.

Inclui bibliografia

1. Física – Teses. 2. Modelo Padrão. 3. Grande Colisor de Hádrons. 4. Física do Charme. 5. Violação de CP. 6. Mapa de Dalitz. I. Göbel Burlamaqui de Mello, Carla. II. Pontifícia Universidade Católica do Rio de Janeiro. Departamento de Física. III. Título.

CDD: 530

To my lovely grandparents José Pachas and Victoria Mora.

Acknowledgments

I am deeply indebted to my advisor Carla Göbel for her invaluable support, encouragement and instructive discussions during the Master Program. I am also thankful for her careful reading of this document and for providing me with the opportunity to carry out this research in her working group.

Since studying abroad has presented some administrative and academic challenges, I have been very fortunate to count on the help of great persons. Indeed, I am grateful to the administrative staff of *Departamento de Física* at PUC-Rio, specially to Professors Hiroshi Nunokawa and Marco Cremona for their guidance during my first months in Brazil. Also, I thank my postgraduate colleagues for the useful discussions and their honest comments during the preparation of this work. Since they come from a wide range of academic backgrounds and nationalities, they have enriched my experience of studying abroad. Likewise, I am thankful to my friends Luis Durand, Carlos Olivares, Edward Quijada and Jimmy Jontop for their support during my first semester in Rio de Janeiro.

I would like to thank my colleagues in the Charm Physics Rio group Josué Molina, Clarissa Baesso and Marcelo Campos for their invaluable suggestions, tireless patience, experience and for providing an excellent working atmosphere. Furthermore, I gratefully appreciate the financial support given by CNPq and FAPERJ during this program.

My deepest gratitude belongs to Diana Gómez for her endless love in spite of the distance. Finally, I want to thank my parents for their encouragement and unconditional support through the good times and through the challenging ones.

Abstract

Pachas Clemente, Javier Alejandro; Göbel Burlamaqui de Mello, Carla. **Search for CP Violation through the $D_s^+ \rightarrow K^- K^+ K^+$ decay in the LHCb Experiment.** Rio de Janeiro, 2015. 85p. Master's Dissertation — Departamento de Física, Pontifícia Universidade Católica do Rio de Janeiro.

This dissertation aims to report the search for charge-parity (CP) violation in the singly-Cabibbo-suppressed decay $D_s^+ \rightarrow K^- K^+ K^+$ at the LHCb Experiment (CERN). According to the Standard Model, direct CP violating asymmetries in charm decays can occur but only up to the order of 10^{-3} or less. If asymmetries at the percent level are found, new CP violation mechanisms beyond the Standard Model are necessary. A model-independent technique known as the Mirandizing method is performed to look for local charge asymmetries in the phase space (the so-called Dalitz plot), of the decay $D_s^+ \rightarrow K^- K^+ K^+$. Our final data sample consists of over 50 thousand events collected in 2012 by the LHCb experiment from proton-proton collisions at a center-of-mass energy of 8 TeV. This is the first time that such analysis is performed to this channel. To guarantee that no nuisance asymmetries appear due to other sources such as background, production or detection effects, the study is first performed to the mass sidebands of the signal as well as to two control channels, $D^+ \rightarrow K^- \pi^+ \pi^+$ and $D_s^+ \rightarrow K^- K^+ \pi^+$, for which no CP violating asymmetries are expected since they are Cabibbo-favored decays. We then analyze the signal sample to find that, under the current statistics, there is no sign of CP violation in the $D_s^+ \rightarrow K^- K^+ K^+$ decay.

Keywords

Standard Model; Large Hadron Collider (LHC); Charm Physics; CP Violation; Dalitz Plot.

Resumo

Pachas Clemente, Javier Alejandro; Göbel Burlamaqui de Mello, Carla. **Busca por violação de CP através do decaimento $D_s^+ \rightarrow K^- K^+ K^+$ no Experimento LHCb.** Rio de Janeiro, 2015. 85p. Dissertação de Mestrado — Departamento de Física, Pontifícia Universidade Católica do Rio de Janeiro.

Esta dissertação tem como objetivo a busca por violação de carga-paridade (CP) no decaimento suprimido por Cabibbo $D_s^+ \rightarrow K^- K^+ K^+$ no experimento LHCb (CERN). De acordo com o Modelo Padrão, assimetrias devido à violação de CP direta em decaimentos de charme deveriam ocorrer a uma taxa menor que 10^{-3} . Se assimetrias da ordem de por cento são encontradas, novos mecanismos de violação de CP além do Modelo Padrão são necessários. Uma técnica modelo-independente, conhecida como método de Miranda, é utilizada para a busca de assimetrias locais de carga no espaço de fase (o chamado Dalitz plot) do decaimento $D_s^+ \rightarrow K^- K^+ K^+$. Nossa amostra final consiste de mais de 50 mil eventos coletados em 2012 pelo experimento LHCb a partir de colisões próton-próton a uma energia de centro de massa de 8 TeV. Esta é a primeira vez que tal estudo é feito neste canal. Para garantir que assimetrias espúrias não estejam contribuindo, oriundas por exemplo de eventos de ruído, ou efeitos de produção ou detecção, o estudo é primeiramente feito às regiões de massa laterais ao sinal e também a dois canais de controle, $D^+ \rightarrow K^- \pi^+ \pi^+$ e $D_s^+ \rightarrow K^- K^+ \pi^+$, para os quais assimetrias de CP não são esperadas já que são processos favorecidos por Cabibbo. Analisamos finalmente nossa amostra de sinal e encontramos que, para a estatística atual, não há evidência de violação de CP no decaimento $D_s^+ \rightarrow K^- K^+ K^+$.

Palavras-chave

Modelo Padrão; Grande Colisor de Hádrons; Física do Charme; Violação de CP; Mapa de Dalitz.

Contents

1	Introduction	14
2	Theoretical Concepts	16
2.1	The Standard Model: A Quick Review	16
2.2	Quantum Chromodynamics	18
2.3	Electroweak Interactions	19
	<i>Cabibbo Theory and the GIM Mechanism</i>	20
	<i>The Cabibbo-Kobayashi-Maskawa (CKM) Matrix</i>	21
	<i>Charge and Parity Symmetries</i>	22
2.4	Introduction to CP Violation	23
2.5	Charm and CP Violation	25
2.6	The Dalitz Plot	27
3	The LHCb Experiment	29
3.1	Particle Detectors	29
3.2	The Large Hadron Collider (LHC)	30
	<i>A Toroidal LHC Apparatus (ATLAS)</i>	31
	<i>Compact Muon Solenoid (CMS)</i>	32
	<i>A Large Ion Collider Experiment (ALICE)</i>	32
	<i>LHC Beauty (LHCb)</i>	32
3.3	The LHCb Experiment	32
	<i>The Trajectory System</i>	32
	<i>Track Reconstruction</i>	36
	<i>Particle Identification</i>	37
	<i>The Trigger System</i>	41
4	Data Selection	43
4.1	Trigger Selection	43
4.2	Stripping Selection	44
4.3	Study of Additional Selection Criteria	45
4.4	Mass-Invariant Fits for each channel	48
	<i>$D_s^+ \rightarrow K^- K^+ K^+$ Channel</i>	48
	<i>Control Channel 1: $D^+ \rightarrow K^- \pi^+ \pi^+$</i>	49
	<i>Control Channel 2: $D_s^+ \rightarrow K^- K^+ \pi^+$</i>	51
5	Search for CP Violation in $D_s^+ \rightarrow K^- K^+ K^+$ Decays	53
5.1	Mirandizing Method	53
5.2	Control Mode 1: $D^+ \rightarrow K^- \pi^+ \pi^+$ Decay	54
	<i>Uniform Binning</i>	55
	<i>Adaptive Binning</i>	57
5.3	Control Channel 2: $D_s^+ \rightarrow K^- K^+ \pi^+$	60

<i>Uniform Binning</i>	61
<i>Adaptive Binning</i>	62
5.4 Background: Mass Sidebands of $K^-K^+K^+$	64
<i>Uniform Binning</i>	64
<i>Adaptive Binning</i>	66
5.5 $D_s^+ \rightarrow K^-K^+K^+$ Signal Region	68
<i>Uniform Binning</i>	69
<i>Adaptive Binning</i>	71
5.6 Summary of the results	73
6 Conclusions and Outlook	74
A Three-particle Decay Kinematics	75
A.1 Kinematic Limits	76
B Definition of Variables for Data Selection	79
Bibliography	82

List of Figures

2.1	Fundamental Interactions	17
2.2	Feynman Diagrams of $D_s^+ \rightarrow K^- K^+ K^+$.	26
2.3	Dalitz plot of $D_s^+ \rightarrow K^- K^+ \pi^+$.	28
3.1	Set of accelerators and detectors at CERN.	31
3.2	The LHCb Detectors	33
3.3	The VErteX LOcator	34
3.4	The Tracking System	35
3.5	Perspective view of the magnet.	36
3.6	Five types of track reconstructions.	37
3.7	RICH System	39
3.8	The Muon System	40
3.9	Muon Stations M1-M5	41
4.1	Mass spectrum for $D_s^+ \rightarrow K^- K^+ K^+$ after stripping and trigger cuts.	45
4.2	The application of PIDK cuts for the 2nd and 3rd particle. The pick is reduced when the cut on PIDK is higher. The colors for cuts in 7, 10, 15, 20, 25 and 30 are black, red, green, blue, yellow and purple, respectively. The horizontal axis in these two plots correspond to $M(K^- K^+ \pi^+)$ (left) and $M(K^- \pi^+ K^+)$ (right).	47
4.3	Invariant-mass distribution of $D_s^+ \rightarrow K^- K^+ K^+$ candidates after the final cuts. The total fit function (blue-line) is shown, with the signal (dashed green) and background (dashed purple) contributions.	48
4.4	Invariant-mass distribution of $D^+ \rightarrow K^- \pi^+ \pi^+$ candidates. The total fit function (blue-line) is shown, with signal (solid green and dashed red) and background (dashed purple) contributions.	50
4.5	Invariant-mass distribution of $D_s^+ \rightarrow K^- K^+ \pi^+$ candidates. The total fit function (blue-line) is shown, with signal (solid and dashed green) and background (dashed purple) contributions	51
5.1	Dalitz Plot of the signal region of $D^+ \rightarrow K^- \pi^+ \pi^+$.	55
5.2	S_{cp} of control channel 1 for 8x8 uniform binning	56
5.3	S_{cp} of control channel 1 for 15x15 uniform binning	56
5.4	Adaptive Binning of a Dalitz Plot in 24 bins.	58
5.5	S_{cp} of control channel 1 for 24 adaptive bins.	58
5.6	S_{cp} of control channel 1 for 64 adaptive bins.	59
5.7	S_{cp} of control channel 1 for 144 adaptive bins.	60
5.8	The Dalitz Plot of $D_s^+ \rightarrow K^- K^+ \pi^+$.	61
5.9	S_{cp} of control channel 2 for 15x15 uniform binning	62
5.10	S_{cp} of control channel 2 for 24 adaptive bins.	63
5.11	S_{cp} of control channel 2 for 64 adaptive bins.	63
5.12	S_{cp} of control channel 2 for 144 adaptive bins.	64
5.13	Dalitz Plot of $D_s^+ \rightarrow K^- K^+ K^+$ in its background region.	65

5.14	S_{cp} of mass sidebands for 8×8 uniform binning	65
5.15	S_{cp} of mass sidebands for 15×15 uniform binning	66
5.16	S_{cp} of mass sidebands of $K^-K^+K^+$ for 24 adaptive bins.	67
5.17	S_{cp} of mass sidebands of $K^-K^+K^+$ for 64 adaptive bins.	67
5.18	S_{cp} of mass sidebands of $K^-K^+K^+$ for 144 adaptive bins.	68
5.19	Dalitz Plot of $D_s^+ \rightarrow K^-K^+K^+$ in its signal region.	69
5.20	S_{cp} of main decay for 8×8 uniform binning	70
5.21	S_{cp} of main decay for 15×15 uniform binning	70
5.22	S_{cp} of main decay for 24 adaptive bins.	71
5.23	S_{cp} of main decay for 64 adaptive bins.	72
5.24	S_{cp} of main decay for 144 adaptive bins.	72
A.1	Dalitz Plot for a three-particle decay	78
B.1	Production process of the meson D_s^+ decaying in $K^-K^+K^+$.	79

List of Tables

2.1	Fundamental Fermions and Bosons	16
2.2	Examples of Baryons and Mesons	18
2.3	Massive electroweak mediators.	20
3.1	Summary of the different systems involved in the LHCb Experiment.	42
4.1	Trigger criteria	44
4.2	Signal and sidebands mass regions used for the CPV studies.	49
4.3	Result of fitting the sample for $D^+ \rightarrow K^- \pi^+ \pi^+$.	50
4.4	$M(K^- K^+ \pi^+)$ fit data.	52
5.1	Results for uniform binning of $D^+ \rightarrow K^- \pi^+ \pi^+$ Dalitz Plot.	55
5.2	Results for adaptive binning of $D^+ \rightarrow K^- \pi^+ \pi^+$ Dalitz plot. Total positives 89,264 and negatives 92,135. ndf = Binning - 1.	60
5.3	Results for uniform binning of $D_s^+ \rightarrow K^- K^+ \pi^+$ Dalitz plot.	62
5.4	Results for adaptive binning of $D_s^+ \rightarrow K^- K^+ \pi^+$ Dalitz plot. ndf = Binning - 1.	64
5.5	Results for uniform binning of the Dalitz Plot of mass sidebands of $K^- K^+ K^+$.	66
5.6	Results for adaptive binning of the Dalitz plot of mass sidebands of $K^- K^+ K^+$. ndf = Binning-1.	68
5.7	Results for uniform binning of $D_s^+ \rightarrow K^- K^+ K^+$ Dalitz Plot in the background region.	70
5.8	Results for adaptive binning of $D_s^+ \rightarrow K^- K^+ K^+$ Dalitz plot in the background region.	73
B.1	Stripping20: Off-line selection criteria for the LHCb data in Run I (2012) for candidates of $D_s^+ \rightarrow K^- K^+ K^+$.	81

*What we achieve inwardly
will change outer reality.*

Plutarch, *Greek historian (AD 46 – 120)*.

1

Introduction

We all live in a Universe that seems to be solely built of what we call *matter*. However, the combination of two of the most fundamental concepts in physics, the special theory of relativity and quantum mechanics, allows the existence of matter of a different kind, known as *antimatter*. In fact, Paul Dirac suggested in 1928 the existence of antielectrons, particles with the same mass and numerically the same charge as electrons $-e$, although with an opposite sign $+e$. These particles were later discovered by Carl Anderson in 1932 and named positrons. Nevertheless, in spite of the presence of antimatter in cosmic rays, the Universe does not contain any significant amount of antimatter [1], suggesting a matter-antimatter asymmetry from an early stage.

Moreover, it was found that the most elementary constituents of matter are point-like particles called quarks and leptons. Indeed, our current understanding of how these particles as well as their antiparticles interact is provided by a theoretical framework known as the Standard Model (SM) [2]. Mathematically, it has not only described the discovered particles, but also has predicted the existence of new ones. Despite its success, however, the recent experimental evidence of neutrino oscillation, dark matter and the baryon (matter-antimatter) asymmetry in the Universe, strongly suggests that the SM is incomplete, that is, there should exist new physics beyond the SM.

We will see that one condition for this matter-antimatter asymmetry to occur in Nature is the violation of the charge-parity symmetry. Initially, antimatter was thought as perfect reflection of matter. Indeed, many phenomena were found to be invariant under conjugation of parity P (spatial reflection) and charge C (transforming a particle to its antiparticle). Yet, the combination of these two symmetries (CP) was found to be violated in weak interactions as reported in 1964 [3]. This first evidence of CP violation (CPV) involved a system of neutral kaons in which a kaon transforms into its antiparticle and vice versa, but such change did not happen with the same probability in both directions (*indirect* CPV). Moreover, it was not until 1999 that experiments in Fermilab and CERN [4] confirmed the presence of CPV in the *decay* of neutral kaons, namely *direct* CPV. Later in 2001, the BaBar (SLAC) [5] and Belle (KEK) [6] experiments observed direct CPV in the decays of *B* mesons containing beauty-flavor quarks.

The LHCb experiment at CERN was mainly designed to study CP violation and rare decays in the beauty sector. However, the characteristics

of its detectors also make suitable the study of charm mesons.

The present dissertation constitutes the first measurement in searching for direct CPV in the single Cabibbo suppressed decay of the charm meson D_s^+ in three charged kaons, $D_s^+ \rightarrow K^- K^+ K^+$, for which there are no references in the literature. Here, the charge conjugation is implied, otherwise it will be explicitly stated. Our data was obtained during Run I (2011 - 2012) from collisions of proton-proton with $\sqrt{s} = 8$ TeV and an integrated luminosity of 2.0 fb^{-1} (2012 data). Indeed, in 2012, unprecedented samples of charm meson decays were collected allowing to get a better statistics than previous years.

The remainder of this dissertation is organized as follows. Chapter 2 presents a quick review of the SM of particle physics. Within this model, the presence of a complex phase in the quark mixing matrix allows the decay amplitude of a particle to be different from the one corresponding to its antiparticle, and, therefore, CP is violated. In the charm sector, CPV is expected to be very small, with asymmetries not greater than 10^{-3} .

Chapter 3 is devoted to describe the LHCb experiment and the role of its components in selecting our sample. Chapter 4 shows the selection criteria and final samples that will be used for our main decay and the control channels, $D_s^+ \rightarrow K^- K^+ \pi^+$ and $D^+ \rightarrow K^- \pi^+ \pi^+$, which are used to ensure that no systematic asymmetry had occurred when taking the data.

A model-independent search for CPV in the phase space or Dalitz Plot (DP) of $D_s^+ \rightarrow K^- K^+ K^+$ is presented in Chapter 5. This approach is called the Mirandizing technique and consists in comparing the distribution of events along the DPs corresponding to D_s^+ and D_s^- . First, we apply this technique to the control channels to make sure that the local asymmetries follow a normal distribution. After that, we study the background of our signal sample. Then, the Mirandizing technique is applied on the signal region of $D_s^+ \rightarrow K^- K^+ K^+$.

The conclusions of this dissertation are summarized in Chapter 6. Finally, Appendix A details the kinematics of a three-body decay and shows how the Dalitz plot is defined.

2 Theoretical Concepts

2.1 The Standard Model: A Quick Review

The Standard Model (SM) is the theory that currently better explains how the ultimate constituents of matter interact. According to the SM, these elementary particles of matter, known as quarks and leptons, interact with one another via the electromagnetic, weak and strong forces. Therefore, the theory includes three out of the four fundamental interactions in Nature, excluding gravity.

The concept of field plays an important role into the SM, since all particles and forces can be consistently described as the quanta of spinor, scalar and vector fields. On the one hand, the quanta of spinor fields are fermions, namely quarks and leptons, which are half-integer spin particles. The quarks are confined forming massive particles known as hadrons, such as the proton and neutron, and come in six flavors: up, down, charm, strange, top and bottom. There are six different leptons: electron, muon, tau and their respective neutrinos. On the other hand, the quanta of vector fields are called vector bosons, with spin 1, and are responsible for carrying the force or interaction between the elementary particles. These bosons are the gluons, the electroweak vectors, W^\pm and Z^0 , and the photon γ . Finally, there is the scalar boson (spin 0), namely the Higgs boson, representing a field responsible for the mass generation of all particles. See Table 2.1 for a list of the fundamental fermions and bosons.

Fermions	Quarks	u	c	t
		d	s	b
	Leptons	e	μ	τ
		ν_e	ν_μ	ν_τ
Bosons	Electroweak	γ, W^\pm, Z^0		
	Strong Force	g		
	Higgs Field	H		

Table 2.1: Fundamental Fermions and Bosons

Technically, the SM is a quantum field theory defined by the local $SU(3) \times SU(2)_L \times U(1)_Y$ gauge symmetry, which fulfills the requirements of unitarity and causality. By construction, the framework of the SM comprises

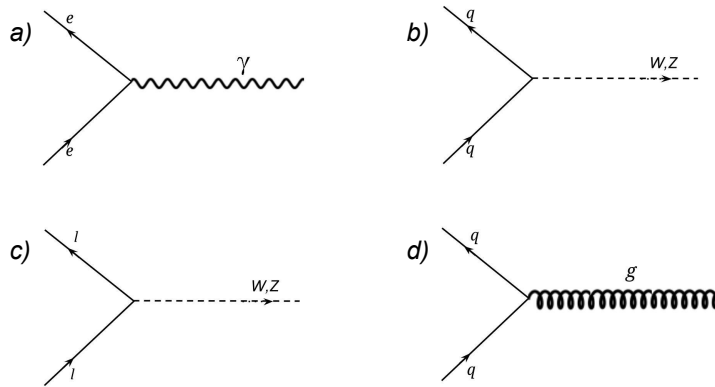


Figure 2.1: The Fundamental Interactions: Feynman diagrams of basic vertex. a) Electromagnetic interaction between an electron and a positron. b) & c) Weak interaction of quarks q and leptons l . d) Strong interaction of quarks.

two theories: the quantum chromodynamics based on the $SU(3)$ symmetry, describing the strong force; and the electroweak theory based on the $SU(2)_L \times U(1)_Y$ symmetry, describing the weak and electromagnetic interactions. Figure 2.1 shows the fundamental interactions represented as Feynman diagrams of their basic vertex [7].

In Nature, all particles come accompanied by their antiparticles, that is, particles with the same mass as their partners but with opposite charge and other additive quantum numbers. For example, for the charged leptons we find the electron and its antiparticle called positron. The antiparticles of quarks (q) are represented with a bar above them as in \bar{q} , where q denotes the first letter of the quark flavor. Neutral particles have also their antiparticles, that is the case of hadron K^0 ($d\bar{s}$) whose antiparticle is made of the antiparticles of d and \bar{s} , namely \bar{K}^0 ($\bar{d}s$).

Created back in 1968, the SM incorporated all the characteristics on the particles known at the time and predicted the existence of new particles as well. Its current formulation has been tested over the years with impressive accuracy. Among its predictions are the discovery of the top quark (1995) [8, 9] and the tau neutrino (2000) [10]. Nonetheless, the most impressive confirmation of the SM has been the discovery of the Higgs boson which was announced by the CMS [11] and ATLAS [12] Collaborations at CERN in 2012.

In the following sections, a brief description of quantum chromodynamics, electroweak interaction and CP violation is presented.

2.2

Quantum Chromodynamics

Quantum Chromodynamics (QCD) is the theory of the strong interaction between quarks. In the framework of the so-called quark model, a hadron consist in either a pair quark - antiquark ($q\bar{q}$) called meson or as a set of three quarks (qqq) known as baryon.¹ Unlike hadrons, it has been found that quarks have fractional electric charges. For instance, quarks u , c , and t have charge $+\frac{2}{3}e$ and quarks d , s , and b have charge $-\frac{1}{3}e$. Therefore, since the structure of a proton is uud , it has an overall electric charge of $+e$. Examples of baryons and mesons are listed in Table 2.2.

Baryons	qqq	Mesons	$q\bar{q}$
Ω^-	sss	π^+	$u\bar{d}$
Δ^{++}	uuu	K^+	$u\bar{s}$
Ξ^-	dss	D^0	$c\bar{u}$
n	udd	D^+	$c\bar{d}$
p	uud	D_s^+	$c\bar{s}$
Σ^+	uus	B^+	$u\bar{b}$
Λ^+	uds	B^0	$d\bar{b}$

Table 2.2: Examples of Baryons and Mesons

Considering the composition of hadrons and the fact that quarks have spin $\frac{1}{2}$, a baryon is a fermion and a meson is a boson. In principle, the quarks forming a particle such as $\Delta^{++}(uuu)$ would be violating the Pauli exclusion principle, which states that two identical fermions can not occupy the same quantum state simultaneously. Thus, it was necessary to introduce a new trait for quarks in QCD allowing the wave function of the hadrons to be antisymmetric even if it is spin-symmetric and flavor-symmetric as in $\Omega^-(sss)$ and $\Delta^{++}(uuu)$. This new property of quarks is known as “color”, in analogy of true color, since they come in three “color charges” red, blue and green. Furthermore, within QCD the interactions of quarks are mediated by massless gluons.

One interesting feature of the strong interaction is that it will remain the same even if the quarks change colors by another, that is, it is invariant under a rotation in color space. Mathematically, this can be stated as that the strong

¹Evidence for the existence of states consisting of 4 quarks (tetraquarks) and 5 quarks (pentaquarks) have been recently reported [13, 14].

interaction holds a $SU(3)$ color symmetry.

$$\left. \begin{array}{l} red \rightarrow green \\ green \rightarrow blue \\ blue \rightarrow red \end{array} \right\} SU(3) \text{ Color Symmetry}$$

The 8 generators of $SU(3)$ would correspond to the 8 massless gluons with spin 1. Furthermore, unlike photons that do not have electric charge, gluons do have color charges themselves, which allows them to interact with one another strongly. It is believed that it is this feature of gluons that increases the strength of the strong interaction at low energies (or large distances). Indeed, the strong coupling α_s is found to increase at low energy and decrease at high energies, a behavior contrary to what happens within Quantum Electrodynamics (QED).

As neither a quark nor a gluon has ever being found experimentally isolated (free), QCD incorporates the concept of confinement by asserting that only color-singlet states (color-neutral) can exist in isolation, then quarks must always be bound into hadrons. For that reason, the three quarks into a baryon have different colors and quark-antiquark pair into a meson have color-anticolor of the same kind as in $u_B\bar{c}_B$.

Therefore, the confinement must be leading to the finite range of the strong interaction at low energies in which non-perturbative methods are necessary. At high energy levels above 2 GeV (α_s small), on the other hand, the study of QCD requires perturbative methods using expansions of α_s . Since the strong interaction becomes weaker at higher energies it is said that QCD exhibits the property of asymptotic freedom.

As we have seen, confinement and asymptotic freedom are two properties of QCD present in different scales of energies. However, the former property has not yet been proven analytically, while the latter was developed by David Politzed, Frank Wilczek and David Gross, laureates with the Nobel Prize in Physics in 2004.

2.3

Electroweak Interactions

A brief introduction to the electroweak theory is presented in this section, since the decays of mesons such as D_s involves a weak interaction.

The weak interaction was discovered in experiments of beta decay. It is responsible for the radioactive decays and for the flavor-change of quarks. The term weak is due to its strength when it is compared with that of the strong or electromagnetic interactions. In the Standard Model, weak and electromagnetic interactions are mixtured by the $SU(2) \times U(1)$

gauge symmetry. This framework is known as the electroweak theory that describes the interaction through three massive mediators, the vector bosons W^+ , W^- , Z^0 and a massless mediator, the photon γ . See Table 2.3.

Boson	Mass (GeV/c ²)
Z^0	91.1876 ± 0.0021
W^\pm	80.385 ± 0.015

Table 2.3: Massive electroweak mediators.

Mathematically, the mixture of electromagnetic and weak interactions by the $SU(2) \times U(1)$ gauge symmetry at high energies would imply the existence of four massless vector bosons corresponding to three W -bosons of weak isospin from $SU(2)_L$ (W_1^+ , W_2^- , W_3^0), and a B^0 -boson of weak hypercharge from $U(1)_Y$. In order to answer why there are three massive mediators and a photon, the SM asserts that the fields associated to these bosons are coupled to a scalar field known as the Higgs field ϕ which suffers of a spontaneous symmetry breaking (SSB), emerging naturally the massive W^\pm , Z^0 and the massless photon γ that are observed at low energies. In particle physics, the SSB of gauge symmetries is best known as the Higgs mechanism and suggested the existence of the recently discovered Higgs boson in 2012.

2.3.1 Cabibbo Theory and the GIM Mechanism

The discovery of new particles in the late 40s suggested the existence of a new quantum number called S (strangeness). This number was conserved in strong and electromagnetic interactions, but not in weak interactions. By that time, it was expected that the coupling constant in weak interaction to be unique (universality of the weak interaction). Experiments of neutron beta decay (semi-leptonic decay in which $\Delta S = 0$) and muon decay (leptonic decay) revealed a similar but not equal value for their coupling constant. Moreover, measurements of branching ratios of processes with $\Delta S \neq 0$ were 10 times greater than in processes with $\Delta S = 0$. Therefore, it appeared that there should be three different coupling constants for these kinds of processes.

In order to preserve the universality of the weak interaction, Cabibbo suggested in 1963 that a hadronic process with $\Delta S = 0$ brings a factor $\cos \theta_c$ and the ones with $\Delta S \neq 0$, a factor of $\sin \theta_c$. In the language of quarks, for example, it is said that the weak charge do not couple the quarks u and d , but the quark u and d' , where d' is a linear combination of the mass states of d and s

$$d' = d \cos \theta_c + s \sin \theta_c, \quad (2.1)$$

then the doublet on which the weak charged interaction acts is actually

$$\begin{pmatrix} u \\ d' \end{pmatrix} = \begin{pmatrix} u \\ d \cos \theta_c + s \sin \theta_c \end{pmatrix} \quad (2.2)$$

where θ_c is called Cabibbo's angle whose value is $2,26 \text{ rad} = 13^\circ$. Therefore, the Cabibbo theory could, then, explain the apparent difference of coupling constants. The transition amplitude \mathcal{M} for each process is associated to the weak coupling constant G_F (Fermi's constant) in the following way

$$\begin{aligned} \text{Leptonic Process} & \quad \mathcal{M} \approx G_F, \\ \text{Hadronic Process } (\Delta S = 0) & \quad \mathcal{M} \approx G_F \cos \theta_c, \\ \text{Hadronic Process } (\Delta S \neq 0) & \quad \mathcal{M} \approx G_F \sin \theta_c. \end{aligned}$$

Later, in 1970, due to the observational absence of flavor-changing neutral currents, Glashow, Iliopoulos and Maiani [15] predicted the charm quark c , introducing a new doublet, the so-called GIM mechanism. Then, another orthogonal mixture would exist between c and s' , where

$$s' = -d \sin \theta_c + s \cos \theta_c \quad (2.3)$$

Then, the first two generations of quarks can be mixed by a Cabibbo Matrix defined as [16]

$$\begin{pmatrix} d' \\ s' \end{pmatrix} = \begin{pmatrix} \cos \theta_c & \sin \theta_c \\ -\sin \theta_c & \cos \theta_c \end{pmatrix} \begin{pmatrix} d \\ s \end{pmatrix} \quad (2.4)$$

which is a real, one parameter unitary matrix.

2.3.2

The Cabibbo-Kobayashi-Maskawa (CKM) Matrix

The wave equation describing how the particles propagates has free-particle solutions known as mass eigenstates. However, the weak interaction between particles occurs through their weak eigenstates, which are linear combinations of mass eigenstates (such in equation 2.1.) The generalization of Cabibbo Matrix 2.4 relating the mass and weak eigenstates, extended to 3 quark generations, is called the Cabibbo-Kobayashi-Maskawa (CKM) Matrix. This unitary matrix is defined as

$$\begin{pmatrix} d' \\ s' \\ b' \end{pmatrix} = \begin{pmatrix} V_{ud} & V_{us} & V_{ub} \\ V_{cd} & V_{cs} & V_{cb} \\ V_{td} & V_{ts} & V_{tb} \end{pmatrix} \begin{pmatrix} d \\ s \\ b \end{pmatrix} \quad (2.5)$$

where the weak interaction would act on the following doublets

$$\begin{pmatrix} u \\ d' \end{pmatrix} \quad \begin{pmatrix} c \\ s' \end{pmatrix} \quad \begin{pmatrix} t \\ b' \end{pmatrix}. \quad (2.6)$$

Being unitary and orthogonal, the CKM matrix has four independent parameters: three mixing angles θ_{ij} and one phase δ . Using a notation of these four parameters, the standard representation of the CKM matrix is

$$\begin{pmatrix} c_{12}c_{13} & s_{12}c_{13} & s_{13}e^{-i\delta} \\ -s_{12}c_{23} - c_{12}s_{23}s_{13}e^{i\delta} & c_{12}c_{23} - s_{12}s_{23}s_{13}e^{i\delta} & s_{23}c_{13} \\ s_{12}s_{23} - c_{12}c_{23}s_{13}e^{i\delta} & -c_{12}s_{23} - s_{12}c_{23}s_{13}e^{i\delta} & c_{23}c_{13} \end{pmatrix}, \quad (2.7)$$

where s_{ij} and c_{ij} are $\sin \theta_{ij}$ and $\cos \theta_{ij}$ respectively. The presence of a complex phase δ in the CKM matrix is responsible for all the CP violation in flavor-changing processes in the SM.

The CKM matrix can also be expressed more suitably as an expansion in terms of $\lambda = s_{12} \approx \sin \theta_c$ to the order $\mathcal{O}(\lambda^4)$ through the Wolfenstein representation that consider experimental measurements

$$\begin{pmatrix} 1 - \lambda^2/2 & \lambda & A\lambda^3(\rho - i\eta) \\ -\lambda & 1 - \lambda^2/2 & A\lambda^2 \\ A\lambda^3(1 - \rho - i\eta) & -A\lambda^2 & 1 \end{pmatrix}, \quad (2.8)$$

The CKM matrix elements are fundamental parameters in the SM and their determination is one of the goal of flavor physics. Finally, depending on the matrix elements contained in its amplitude, a weak decay is said to be

- Cabibbo Favored: only diagonal terms,
- Singly Cabibbo Suppressed: one factor of V_{us}, V_{cb}, V_{cd} or V_{ts} ,
- Doubly Cabibbo Suppressed: two of the previous factors, or one of V_{ub} or V_{td} .

2.3.3

Charge and Parity Symmetries

In the SM just twelve fermions are enough to describe matter and its fundamental interactions (see Table 2.1). Based on their similar properties, these fermions are grouped into three families or generations as it is shown below

$$\begin{pmatrix} u \\ d \\ e \\ \nu_e \end{pmatrix}, \begin{pmatrix} c \\ s \\ \mu \\ \nu_\mu \end{pmatrix}, \begin{pmatrix} t \\ b \\ \tau \\ \nu_\tau \end{pmatrix} \quad (2.9)$$

Among these generations, the components of the first one make up most of the known matter around us.

Quarks and leptons are massive fermions that present a property called helicity. A particle is said to be right-handed if its momentum and spin have

the same direction, while a left-handed particle has its momentum and spin in opposite directions. Mathematically, these massive fermions can be described by Dirac spinors ψ which can be separated in left- and right-handed states after the application of projection operators [17] such in

$$\psi_L = \frac{(1 - \gamma^5)}{2}\psi, \quad \psi_R = \frac{(1 + \gamma^5)}{2}\psi. \quad (2.10)$$

The initial attempts to form an electroweak theory assumed that the weak interactions were invariant under a spatial reflection of particle positions, that is, the description of the interaction do not change if the particle positions \vec{r} are replaced by their opposite $-\vec{r}$. The latter is done under the parity operator P, which reverse the positions of a four-vector and leave its time component unchanged. A parity operation would reverse the momentum of a particle but not its spin and, therefore, it would convert a left-handed particle in a right-handed one. Experimentally, strong and electromagnetic interactions obey *parity symmetry*. However, weak interactions violate parity symmetry, as it was suggested in a 1956 by Lee and Yang [18] and experimentally verified in 1957 by Wu et. al. [19] in Cobalt-60 beta decays.

The *charge symmetry* (C) in fundamental interactions is also an important physical concept. In this case, this symmetry occurs if an interaction is invariant under an exchange of particles by their antiparticles. As in the case of P-symmetry, C-symmetry is not violated in strong and electromagnetic interactions, but it is violated by the weak interaction.

Although individually violated by the weak interactions, the application of charge and parity symmetries together, namely CP symmetry, was expected to be a fundamental symmetry in Nature. However, it was in 1964 that the discovery of CP violation in the decays of neutral kaons was found [3]. This CP asymmetry is discussed in more detail in the following section.

2.4

Introduction to CP Violation

One of the fundamental questions in Physics is why there seems to exist more matter than antimatter in the Universe. This question arises because it is assumed that particles and antiparticles were created in the same amount in the early Universe and these would have annihilated with each other completely, but the experimental evidence shows that the solar system and distant galaxies as well are made up of the same material as the Earth. We can conclude, therefore, that the baryon number B in the Universe is greater than zero ($B > 0$).

Three possible explanations for the last conclusion have appeared [20].

The first is that the Universe has always been baryon-asymmetric, that is, $B > 0$ just after the Big Bang and nothing has changed since then. However, thermodynamic considerations suggest that an initial asymmetry would be eliminated. Another possibility is that the Universe is actually baryon-symmetric, that is, $B = 0$ since the Big Bang until now. Initially, then, the Universe had expanded fast enough that matter and antimatter could not annihilated completely. As a consequence, there should be regions in outer space formed by clumps of matter and antimatter, producing an annihilation radiation. Also, high-energy cosmic rays should be made of matter and antimatter with almost the same probability. Nevertheless, no isotropic annihilation radiation has been detected, neither the amount of protons in cosmic rays is close to the number of antiprotons ($10^4 : 1$). Currently, it is accepted a third possibility, the Universe started with $B = 0$ and then some mechanisms have changed this condition, allowing the generation of baryons. In 1967, Sakharov [21] proposed three conditions to explain the baryogenesis mechanism.

1. *At least one process did not conserve the baryonic number* when the baryons were created. This condition would suggest, for example, the decay of protons which has not yet been observed.
2. Since the Boltzman distribution dictates that the number of particles and antiparticle are the same in thermal equilibrium, some *interactions might have occurred outside the thermal equilibrium*.
3. If charge symmetry (C) is a Nature's symmetry, then, baryon number violation would not be enough. If C is conserved, then every reaction violating the baryon number (B) is as likely as its C-conjugate.

$$\Gamma(X \rightarrow Y + B) = \Gamma(\bar{X} \rightarrow \bar{Y} + \bar{B})$$

As both reactions have the same rate, the total baryon number is going to conserve. Therefore, *C-violation is a Sakharov's condition*. Nevertheless, this condition is not enough since an eventual reaction violating the B -number $X \rightarrow q_L q_L$ would create left-handed baryons. Analogously, if CP is a Nature's symmetry, then, the last reaction is as likely as its CP-conjugate $\bar{X} \rightarrow \bar{q}_R \bar{q}_R$. The B -number would be conserved since the following relation is hold, even if the C-conjugates may not have the same rate,

$$\Gamma(X \rightarrow q_L q_L) + \Gamma(X \rightarrow q_R q_R) = \Gamma(\bar{X} \rightarrow \bar{q}_R \bar{q}_R) + \Gamma(\bar{X} \rightarrow \bar{q}_L \bar{q}_L)$$

Therefore, *CP should also be violated* to ensure that the production of baryons (B) exceeds the production of antibaryons (\bar{B}).

CP violation indicates a difference in the decay rate of a particle to a final state and the one related to its antiparticle decaying in a CP-conjugate final state. In order for this difference to occur, there should be at least two ways (channels) in which a particle can decay to a given final state. Then, CPV arises as the amplitude interference of these channels through strong and weak phases. In fact, this scenario can occur in our channel of interest, D_s meson decaying to three kaons, through two different processes which are schematically represented by the Tree and Penguin Feynman diagrams (see Figures 2.2).

There are two kinds of CP violations. The indirect CPV occurs when a particle mixes with its antiparticle (through exchanges of W bosons) and decays in a CPV eigenstate. This kind of decay occurs, for example, in the neutral meson mixing of K^0 and \bar{K}^0 [3]. A CPV is said to be direct when a particle decays in a different rate than the one corresponding to its antiparticle. The first suggestion of this kind of CPV was reported by the NA31 Collaboration in 1988, but experimentally confirmed by Fermilab and CERN in 1999 [4]. Furthermore, in order to have a quantitative measure of CPV, a quantity called direct CPV asymmetry (A_{CP}) is defined as

$$A_{CP} = \frac{\Gamma^+ - \Gamma^-}{\Gamma^+ + \Gamma^-} \quad (2.11)$$

where Γ^+ (Γ^-) is the decay rate of the particle (antiparticle) and can be measured experimentally. Despite CPV is not sufficient to explain the excess of matter over antimatter in the Universe, it is actually necessary, which makes it an important area of current research. In particular, the next section is concerned with CPV in charm meson decays.

2.5

Charm and CP Violation

The weak decay is a source of CPV study since all of them are unstable. In particular, we are concerned with the decay of so-called charm mesons ($c\bar{q}$) such as D_s^+ ($c\bar{s}$) and D^+ ($c\bar{d}$), whose masses are 1969 and 1869 MeV/ c^2 , respectively. CP violation through charm meson decays requires the interference of two amplitudes to the same final states with different strong and weak phases. However, these amplitudes must have similar magnitudes in order for their interference to be appreciable [22]. Single Cabibbo-suppressed decays such as our channel $D_s^+ \rightarrow K^- K^+ K^+$, present the interference between alternative mechanisms through which it can occur and are represented by tree and loop Feynman

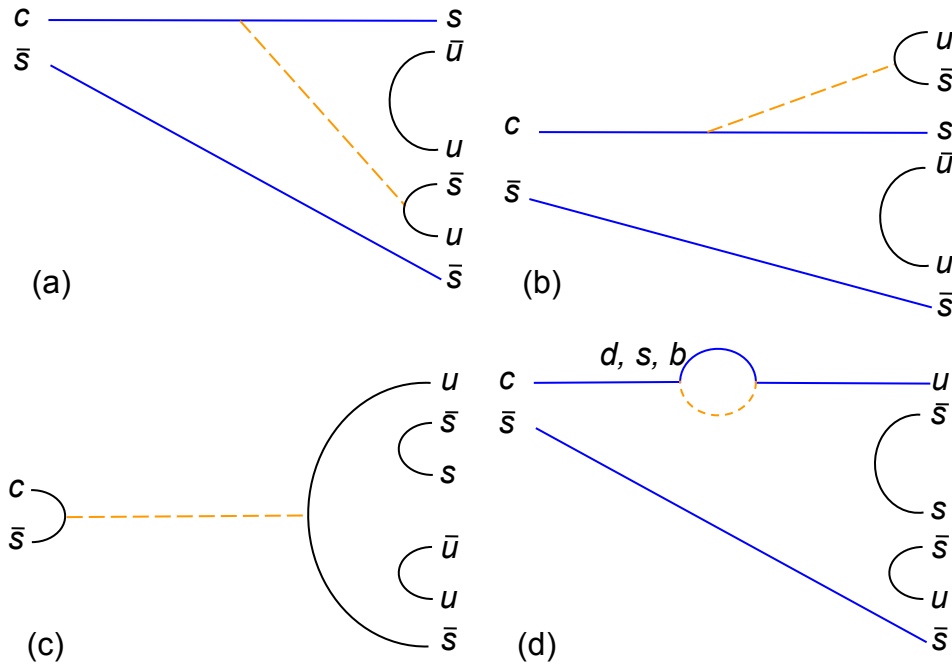


Figure 2.2: Some Feynman Diagrams of $D_s^+ \rightarrow K^- K^+ K^+$. The internal and external emission of a W vector boson (yellow line) that eventually transforms in the pair $u\bar{s}$ are shown in tree diagrams (a) and (b), respectively. (c) represents a possible annihilation process of the pair $c\bar{s}$. The transition $c \rightarrow u$ through a loop is represented in the penguin diagram (d) in which a gluon (not shown) creates the pair $s\bar{s}$.

diagrams. The tree diagrams, nevertheless, largely dominate over the penguin diagrams, making CPV expected to be tiny within the SM.

The possible diagrams for the decay $D_s^+ \rightarrow K^- K^+ K^+$ are shown in Figure 2.2. According to the Feynman rules, diagrams (a), (b) and (c) contribute with the same CKM elements $V_{cs}^* V_{us}$, while (d) presents a linear combination of $V_{cb}^* V_{ub}$, $V_{cs}^* V_{us}$ and $V_{cd}^* V_{ud}$. The former term $V_{cb}^* V_{ub}$, however, carry a weak phase. The relevance of these processes resides in them being sensitive to CPV effects which the SM foresees only a small magnitude ($<0.1\%$) for the charm sector.

In the next section we are going to study how the distribution of events over the phase space of a decay is related with its rate. Indeed, it is through an analysis of local differences in the distribution of events along these spaces or Dalitz Plots for D_s^+ and D_s^- that our search for CP violation is based.

2.6

The Dalitz Plot

Our main decay $D_s^+ \rightarrow K^- K^+ K^+$ is an example of a three-body decay whose analysis is preferably developed in the mother rest frame. Unlike two-body decay where daughter particles would have fixed momenta, a three-body decay would require that the daughters will be produced in a same plane and that, for spinless mother and daughters, the final state has two degrees of freedom. Thus, we would have three different ways to group these daughter particles in pairs. If we group, for example, particles 1 and 2, and define an invariant mass for this pair as m_{12} , where $m_{12}^2 = (P_1 + P_2)^2 = (P_M - P_3)^2$ and P_i is the four-momentum of particle i in the same mother rest frame, then any two of these invariant masses m_{12} , m_{13} , m_{23} would be enough to completely describe the kinematics of this decay process. A more detailed treatment of the kinematic aspects of a three-body decay is found in Appendix A, where m_{ij}^2 is defined as s_{ij} and the scatter plot of s_{12} versus s_{13} is referred as a Dalitz plot.

The partial decay rate of a particle of mass m_M in its rest frame is given in terms of the Lorentz-invariant matrix element \mathcal{M} by [23]

$$d\Gamma = \frac{1}{(2\pi)^3} \frac{1}{32m_M^3} |\overline{\mathcal{M}}|^2 ds_{12} ds_{13}, \quad (2.12)$$

where $ds_{12} ds_{13}$ is a differential element of the Dalitz plot, $|\overline{\mathcal{M}}|^2$ is the matrix element and involves the decay dynamical aspects, however all the kinematic factors are included into the coefficient in the front. Thus, we can deduce that if $|\mathcal{M}|^2$ is constant, the Dalitz plot would be populated uniformly with events within the allowed kinematic limits. Thus, any variation in the population of the Dalitz plot provides information on $|\mathcal{M}|^2$ and might indicate the presence of two-body resonances as intermediate states.

As an example, Figure 2.3 shows a Dalitz plot of $D_s^+ \rightarrow K^- K^+ \pi^+$ in logarithmic scale for the LHCb data sample, as will be further discussed in Chapter 5.

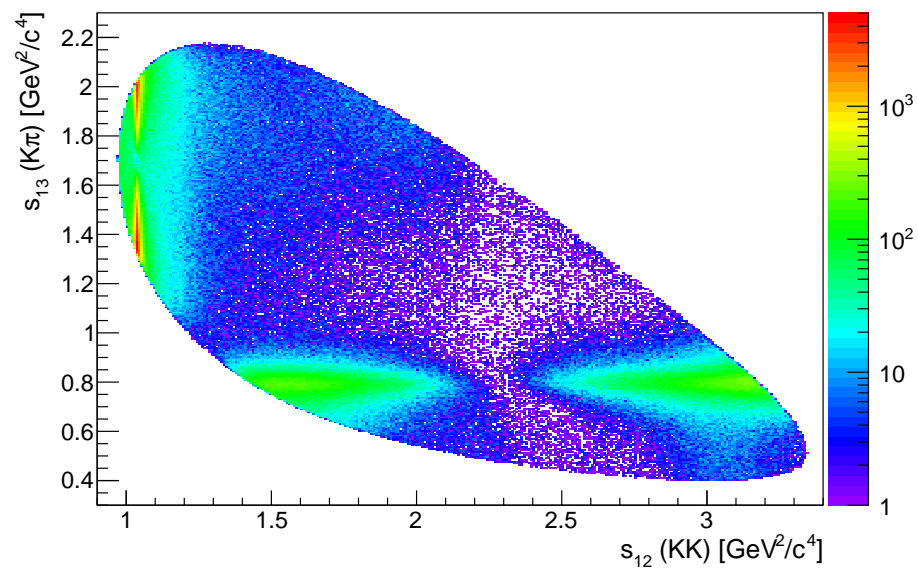


Figure 2.3: Dalitz plot of $D_s^+ \rightarrow K^- K^+ \pi^+$. Around a million of events shown in logarithmic scale.

3

The LHCb Experiment

The discovery of elementary particles has always been a challenge, a close interplay between theoretical expectations and experimental resources. In this chapter, we provide a description of the experimental setting in which our concerning D_s meson decay takes place. We begin with a brief discussion of particle detectors and their main features. Then, an introduction to the Large Hadron Collider and its diverse experiments is presented. Further ahead, we conclude with a more detailed description of the detectors particularly involved in the LHCb experiment.

The present work is based on data collected in the LHCb 2012 run. However, the LHC detectors have been updated since then. Now in 2015, the LHC is able for example to study events at a maximum energy of 13 TeV. Therefore, we present a description of detectors as for the 2012 set-up.

3.1

Particle Detectors

Each time higher levels of energy are needed to find out the particular features of elementary particle interactions. Such energies are achieved, for example, by colliding stable particles, after they were accelerated to ultra-relativistic speed, close to the speed of light. After the collisions, many particles are produced, leaving traces of their pass through the different detectors. Each detector is specifically designed to reveal key characteristics such as trajectory, energy, momentum and mass. Among the most important types of detectors are the tracking devices, calorimeters and particle-identification detector [24, 25].

The **tracking devices** allow to get the path followed by charged particles. The mechanism of many tracker detectors is based on the movement of polarized atoms/molecules induced by the charged particles, then, a charge drift is created and used as signal. Other trackers work with the trails of ions that can also be produced, those electrical signals are recorded for a posterior reconstruction of their trajectories.

A **calorimeter** measures the energy lost by a particle when passing through it. It is designed to absorb the full kinetic energy of a particle and supplies an electrical signal proportional to the energy deposited into the detector. Some calorimeters consist of layers of high-density material such as lead. Indeed, they are able to measure the energy of electrons, photons and

hadrons. However, a calorimeter is not able of stopping particles such as muons or neutrinos, since they have a weak interaction with matter.

The **particle-identification detectors** take advantage of the type of radiation emitted by charged particles. On the one hand, when a charged particle travels faster than light does in the same dielectric medium, it emits Cherenkov radiation at a given angle which is determined by its velocity. This velocity along with a measure of momentum allows to get the particle's mass. On the other hand, when a charged particle traverses the limit between two electrical insulators with different electric resistances, it emits a so-called transition radiation which is particularly characterized by its energy and therefore, its identity.

As we are going to see in the following sections, an experiment of high energy physics usually involves the synergy of various types of detectors. In fact, the clues provided by them are invaluable information on the ultimate constituents of matter.

3.2

The Large Hadron Collider (LHC)

The LHC is the world's largest and more complex particle accelerator. It is localized in Geneva, Switzerland, and is operated by the European Organization for Nuclear Research (CERN), of which Brazil is one of the countries with co-operation agreements.

The LHC tunnel was build underground with a depth ranging from 50 to 175 meters. The main goal of this accelerator is to collide high-energy particle beams traveling in opposite directions along a 27 km ring of superconducting magnets.

The accelerator operation has implied a technical and scientific endeavor never done before. For instance, before the collision, the beams are contained into two tubes (beam pipes) at ultra-high vacuum and at a low temperature of -271.3°C , allowing the particles inside them to move close to the speed of light and, therefore, achieve high-energy levels. Thousands of superconducting magnets are used to conduct the particles through strong magnetic fields along the ring, for example 1232 dipole magnets are responsible for bending of the beams, while 392 quadrupole magnets enable the focus of the beams.

The LHC pursuits an ambitious scientific agenda [26] and has specially designed detectors to accomplish it. Its agenda includes the search for the origin of mass (mainly ATLAS and CMS), matter-antimatter asymmetry (mainly LHCb), dark matter (ATLAS and CMS), and the study of the quark-gluon state (mainly ALICE).

The LHC was designed to collide protons with a maximum center-of-mass energy of 14 TeV. On September 10, 2008, it started up with the circulation of proton beams in its main ring. Unfortunately, the rupture of a liquid helium enclosure caused the damage of over 50 superconducting magnets, delaying the operation for 14 months. Then, on November 23, 2009, the first proton-proton collision was recorded at an injected energy of 450 GeV per beam and on March 30, 2010, collisions of beams, each with energy 3.5 TeV, took place. In the 2012 run, the LHC achieved collisions of protons with $\sqrt{s} = 8$ TeV [27]. This first cycle of operation 2010 - 2012 is known as Run I. Now in 2015, it is starting the Run II with $\sqrt{s} = 13$ TeV. A brief discussion of the different experiments is presented below, see Figure 3.1.

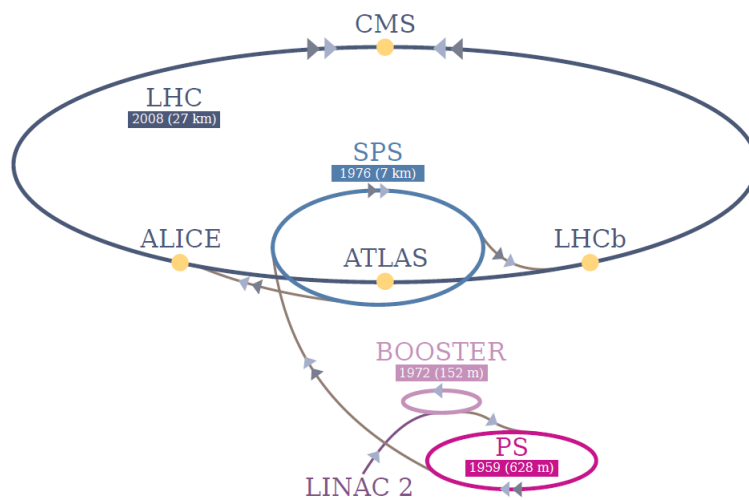


Figure 3.1: Set of accelerators and detectors at CERN.

3.2.1

A Toroidal LHC Apparatus (ATLAS)

ATLAS is the largest particle detector in the world with almost 25 m in height and 44 m in length. Because its main goal is to look for any sort of new physics, this detector is a general-purpose detector. Therefore, studies such as supersymmetry, extra dimensions and dark matter have been developed in this detector due to the high levels of energies available at the LHC. In fact, on July 2012, ATLAS reported the discovery of the *Higgs Boson*, a missing particle into the Standard Model which would explain the mechanism by which other fundamental particles gain their masses.

3.2.2

Compact Muon Solenoid (CMS)

CMS shares the same objectives as ATLAS with a different set-up, using muon detectors and a solenoid magnet. It is also called a general-purpose detector and was designed to corroborate new findings at the LHC. Indeed, both collaborations, ATLAS and CMS, announced the Higgs discovery together.

3.2.3

A Large Ion Collider Experiment (ALICE)

According to Quantum Chromodynamics, there should be a new phase of matter at extremely high temperatures and densities. Then, ALICE aims to study this new phase called *quark-gluon* plasma (QGP) by colliding heavy ions such as $Pb - Pb$ and $p - Pb$. Indeed, it is thought that at the very first milliseconds after the Big Bang, the whole Universe would have been in a QGP state where the quarks were almost deconfined.

3.2.4

LHC Beauty (LHCb)

During the early stage after the Big Bang, an asymmetry between matter and antimatter should have been created, otherwise the Universe would consist only of photons, product of the eventual symmetry. However, our own existence proves that this is not the case. What makes, then, a particle different from its antiparticle at a fundamental level? These kind of questions are the ones the LHCb experiment was built to help answering. It studies this subtle asymmetry through measurements of CP violation and rare decays of beauty and charm hadrons, namely heavy flavor physics. Because this dissertation deals mainly with D_s meson decays in the LHCb experiment, a description of its detectors is presented in the following sections, see Figure 3.2.

3.3

The LHCb Experiment

3.3.1

The Trajectory System

This LHCb system is formed by a Vertex Locator detector (VELO), the LHCb Magnet and four trackers (TT and T1-T3). The first detector allows to identify interaction points (vertex) as well as the trajectories, the Magnet is used to deflect the trajectory of electrically charged particles (actually, once the magnet orientation is fixed, the positive or negative charge of a given particle is deduced

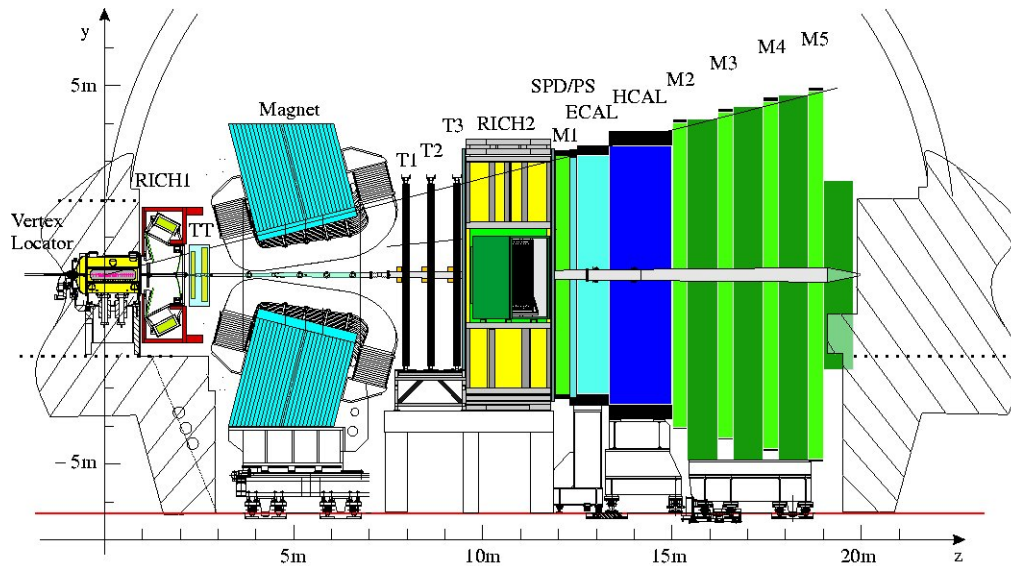


Figure 3.2: The LHCb and the location of its different detectors.

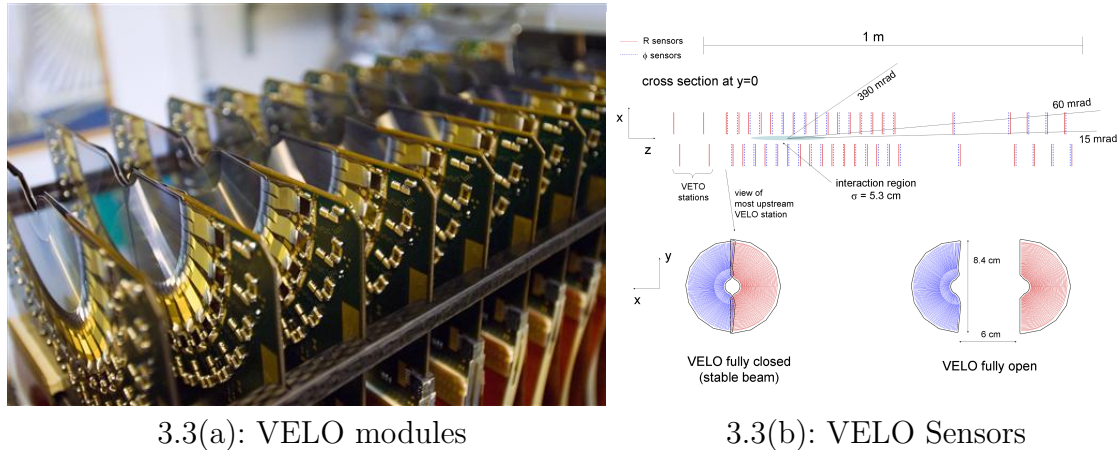
from the deflection of its trajectory). Finally, the trackers help to determine momentum of a particle. These detectors are discussed below.

Vertex LOcator (VELO)

After the proton beams collide, hundreds of particles are produced. The first step to know the trajectory of these particles is to locate where the interaction point has taken place. For this purpose, the VELO detector [28, 29] surrounds the area in which the proton beams collide. Since the detector is made of silicon micro-strips, it is able to provide accurate measurements of the interaction-points coordinates, known as Primary Vertex (PV). These measurements are also used to find the Secondary Vertices (SV). For example, when a D meson is created at the PV, it travels a short distance before decaying at the SV into other mesons. In this sense, VELO allows measurements of B and D meson lifetimes and impact parameters. For the localization of the VELO detector see Figure 3.2.

The VELO detector is made of silicon strips and consists of 42 planar modules. Each module has two sensors, R-sensor on one side and a ϕ -sensor on its opposite side, the former measures radial coordinates and the latter, azimuthal coordinates. Then, the modules are arranged in pairs forming stations, in such a way that an R-sensor from one module is next to a ϕ -sensor of a second module. Therefore, a total of 21 stations are placed along the beam axis (z axis). The information provided by the sensors, along with the position of a given station, makes possible a 3-D reconstruction of tracks and vertices.

Furthermore, the resolution for a PV (SV) is $40\ \mu\text{m}$ ($150\ \mu\text{m}$) in the beam axis and $10\ \mu\text{m}$ ($300\ \mu\text{m}$) in the ϕ direction. However, the vertex resolution strongly depends on the number of tracks in the vertex. For example, a resolution of $13\ \mu\text{m}$ in the transverse plane and a $71\ \mu\text{m}$ along the beam axis is achieved for vertices with 25 tracks [30]. Figure 3.3 shows a lateral view of VELO modules and their R- and ϕ -sensors.



3.3(a): VELO modules

3.3(b): VELO Sensors

Figure 3.3: The VERTex LOcator detector: (a) A lateral view of the modules from one side. (b) Schematic representation the R- and ϕ -sensors (semicircles) into a station, each containing 2,048 strips in radial angular arrangements, respectively. A layout of the stations is also shown in the RZ plane.

Tracking System

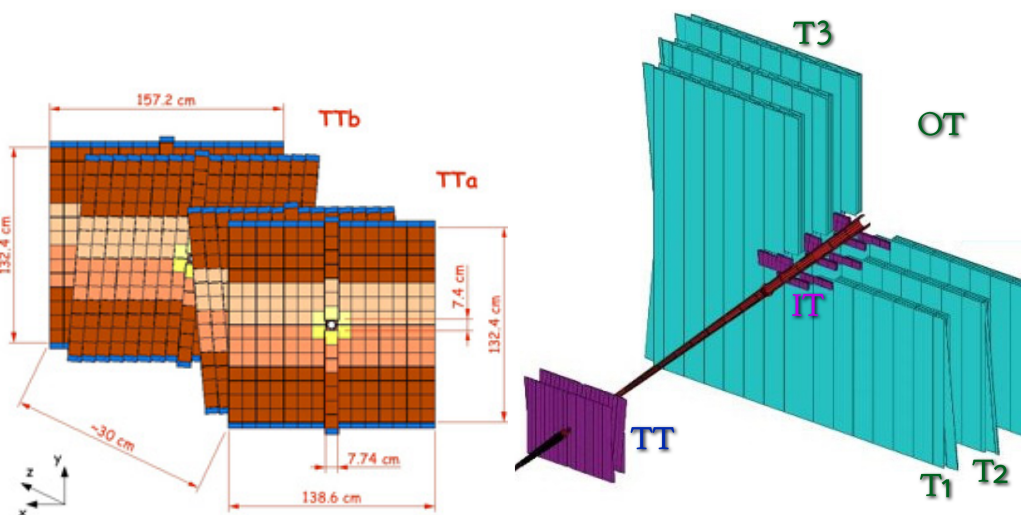
This system provides an efficient reconstruction of charged-particle tracks which are used to determine a particle's momentum. Moreover, the information obtained is later used for the reconstruction of the Cherenkov rings by the RICH System [31]. The system consists of three detectors

- **Tracker Turicensis (TT)** provides information on the tracks left by particles with low momentum. It is a planar tracking station (150 cm wide, 130 cm high) and covers the full acceptance of the experiment. This detector is localized between RICH 1 and the Magnet. Further, it comprises four silicon layers which are arranged as shown in Figure 3.4(a), where the two inner layers are rotated -5° and $+5^\circ$ to provide a better resolution of transverse momentum.
- **Inner Tracker (IT)** [32] covers about 120 cm wide and 40 cm high cross-shaped region in the center of three large planar tracking stations (T1, T2 and T3) downstream of the magnet. Despite its small area when

compared with the outer tracker, it receives around 20% of the total flux of particles, see Figure 3.4(b).

- **Outer Tracker (OT)** [33] covers the largest fraction of the detector sensitive area (600 cm x 490 cm) in stations T1-T3. It helps to detect tracks inside the LHCb acceptance and with angles greater than 15mrad. Each OT has a modular design, that is, they are built from 72 separate modules supported on four independently moving aluminum frames (18 modules per frame). Figure 3.4(b) shows the layout of the IT and OT detectors.

Meanwhile, the TT and IT detectors form the so-called **Silicon Tracker** [34] because both detectors use silicon microstrip detectors with long readout strips. This tracker has a sensitive surface of approximately 11 m² and can measure the position of a particle with a resolution of 0.05 mm.



3.4(a): Tracker Turicensis (TT)

3.4(b): VELO Sensors

Figure 3.4: The Tracking System: (a) Display of the TT layers with their rotation of $\pm 5^\circ$ (b) The inner (IT) and outer (OT) trackers.

The Magnet

The magnet consists of a dipole that allows to measure the charge and linear momentum of charged-particles by determining the deflection of their trajectories. Further, the magnet has two trapezoidal coils producing an integrated field of 4 Tm for 10 m of track length and covers an angular distance of ± 250 mrad vertically and ± 300 mrad horizontally [35]. In order to reduce systematic errors, the magnet is also able to change its polarity. Then, it is

possible to take data with the field in the UP direction (*MagUp*) or DOWN direction (*MagDown*). It is convenient to work with a right-handed coordinate system in which the interaction point is the origin, the z -axis is along the beam direction and the y -axis points upward. A perspective view of the magnet at the LHCb is shown in Figure 3.5.

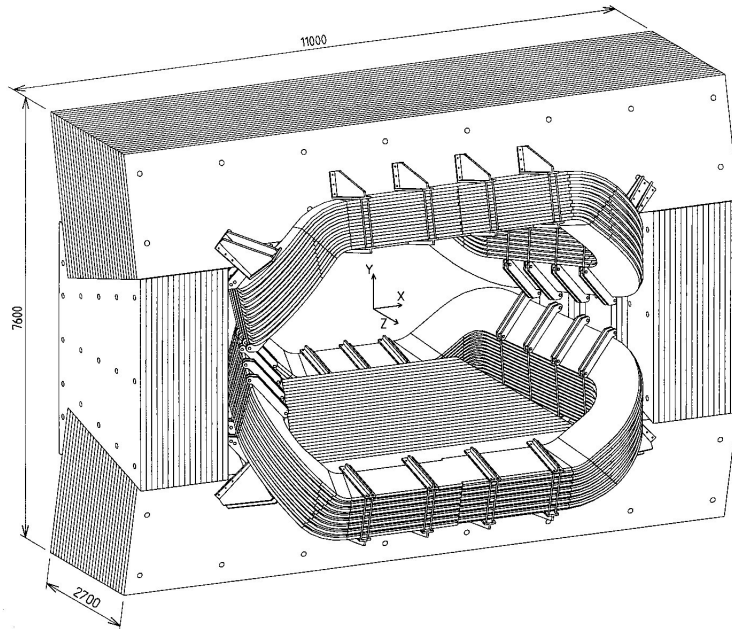


Figure 3.5: Perspective view of the magnet.

3.3.2 Track Reconstruction

All the information provided by the previous detectors allows to reconstruct the possible trajectories. Such reconstruction is made through an algorithm called Kalman-Filter method, which relies on a progressive update of the fit of the trajectory. This feature increases our knowledge of the track without the need to restart a complete fit.

The reconstruction process starts by a 2D pattern recognition, which is made in the RZ plane (fixed ϕ). On the same side of the VELO detector, the algorithm correlates the hits left in two modules (R sensors), which are separated at least for two stations. The hits of these kind are saved in a cluster of possible straight tracks. This cluster is complemented with the information on the azimuthal angles in the different modules (ϕ sensors), allowing a 3D reconstruction of the tracks as indicated in reference [36]. Finally, the trajectories can be divided in five groups, depending on which

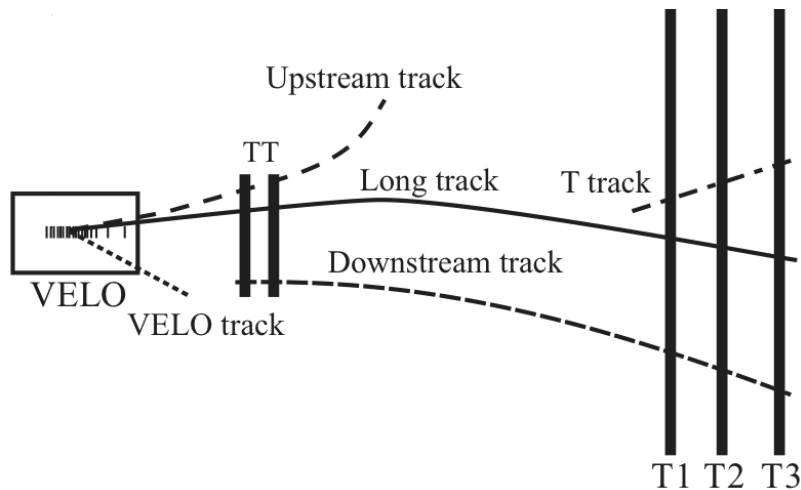


Figure 3.6: Five types of track reconstructions.

detectors are involved in their reconstruction. Figure 3.6 shows these five types of reconstructed tracks.

- **VELO tracks** are left by particles escaping the detector acceptance just after hitting the VELO sensors.
- **Upstream tracks** indicate particles passing through the VELO detector and the TT station.
- **Downstream tracks** are left by particles only passing through TT and T1-T3 stations. Such tracks are, in general, produced by decays taking place outside VELO.
- **Long tracks** correspond to particles with high momentum, hitting most of the detectors.
- **T tracks** are mainly produced by secondary interactions. These tracks are reconstructed in T1, T2 and T3 stations.

3.3.3 Particle Identification

Particle Identification (PID) is crucial to reduce background when selecting the final states. Since we are looking for CP violation in charm mesons decay, it is essential to be able to distinguish, for example, between kaons and pions (common products of charm meson decays). The detectors involved in particle identification are RICH, Calorimeters and Muon systems, therefore, a review of each one is presented below.

RICH System

The Ring-Imaging Cherenkov (RICH) System [31] works together with the Tracking System to identify charged particles in a momentum range of 1-150 GeV/ c and angular acceptance of 10-300 mrad. As it was introduced in section 3.1, when a particle emits Cherenkov radiation, it does as a cone forming an angle θ_c with its track such that

$$\cos \theta_c = \frac{1}{vn} \quad (3.1)$$

where θ_c is known as the Cherenkov angle, v is the particle's velocity and n is the refractive index of the medium. Once the velocity is obtained, the information coming from the tracking system about the momentum is used to determine the particle's mass. A remarkable feature of the created particles after a high energy collision is that the smaller (greater) the angle they are scattered, the higher (lower) their momentum. For this reason, the RICH System consists of two subsystems that are sensible to momenta range.

- **RICH 1** is used to identify charged particles with low momentum (2-60 GeV/ c) and is found between VELO and TT. Here, Silica aerogel (SiO_2) with $n = 1.03$ and Fluorobutane (C_4F_{10}) with $n = 1.0014$ are used.
- **RICH 2** is used to identify charged particles with relatively high momentum (15-150 GeV/ c). It is localized behind the magnet and the tracking system. RICH 2 uses CF_4 with $n = 1.005$.

The RICH System uses spherical (RICH 1) and plane mirrors (RICH 2) to deflect the Cherenkov light, focusing it into Hybrid Photon Detectors (HPD). Then, photo-electrons generated in these detectors are accelerated to amplify their signal. Finally, a particle is identified when the information concerning the hits on HPD, its track reconstruction and its expected behavior has been confirmed.

Figure 3.7 displays a lateral view of the RICH System. The longitudinal scale below shows how far the subsystems are from the collision point. See Figure 3.2 to notice the difference in size between them.

Calorimeter System

In the LHCb experiment, the main function of the calorimeter system is to help in the particle-identification such as electrons, photons and hadrons, since this system is capable to measure the position and energy of these particles. Indeed, the information on the candidates' transverse energies (calculated from

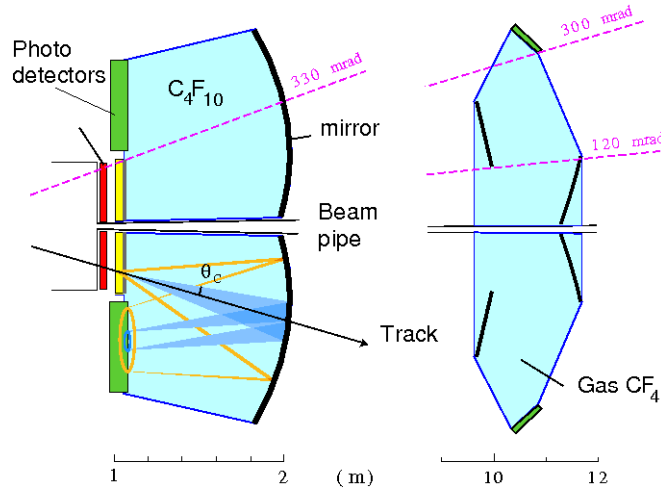


Figure 3.7: Lateral view of the RICH System. RICH 1 (left) and RICH 2 (right).

the perpendicular component of the particle's momentum) is sent to the L0 Trigger, which takes a decision $4 \mu\text{s}$ after the interaction.

A calorimeter measures the total energy left by the particle in the medium. In fact, a shower of new particles with lower energies is produced after the initial particle has traveled a distance X_0 (radiation wavelength). The new particles pass through scintillators inducing the generation of photons that are collected into photomultiplier tubes. In this sense, a calorimeter can determine the energy of an initial particle.

The system is formed by an electromagnetic calorimeter (ECAL), a hadronic calorimeter (HCAL), a Scintillating Pad Detector (SPD) and a Pre-Shower Detector (PS) [37].

- The ECAL measures the energy of electrons and photons and makes the reconstruction of π^0 s. It is formed by a 2 mm lead sheet, 4 mm scintillator boards and a white layer to avoid reflexions on the scintillator. The typical resolution for an energy E is given by $10\%/\sqrt{E} \otimes 1\%$.
- The HCAL measures the energy of protons, neutrons, pions and kaons. Unlike ECAL, HCAL uses the nuclear interaction length λ (greater than the radiation length) to determine the hadronic showers and its scintillators are parallel to the particles beam. The HCAL is formed by 4 mm scintillator boards and 16 mm iron sheets. A typical resolution for an energy E is given by $80\%/\sqrt{E} \otimes 10\%$.
- The SPD helps to reject electrons with high transverse momentum, being its main role to discriminate e^- and γ - showers. Also, it helps the ECAL

to reject background of neutral pions π^0 and γ from the selection of electrons.

- The PS (with information coming from ECAL) rejects the background of charged pions π^\pm from the candidates to electrons. Both, SPD and PS, are separated by a 15 mm lead sheet and consist of two scintillator sheets. They are located before the ECAL.

Muon System

The detection of muons is important at the LHCb experiment because they are also present in the final state of many B and D meson decays. The system has five stations (M1 - M5) that gradually covers a total area of 435 m². In order to guarantee the absence of other particles (hadrons, electrons and photons), some iron filters are interleaved between these stations (Figure 3.8). In this system, the stations have chambers containing a mixture of gases, CO₂, Ar and CF₄. Therefore, when the muons pass through the gases (ionization), the formed ions move forward to wire electrodes with opposite sign, generating a small current that can be amplified and detected, this technology is called Multi-Wire Proporcional Chamber (MWPC). Then, the position where a muon hit a station has been identified [38].

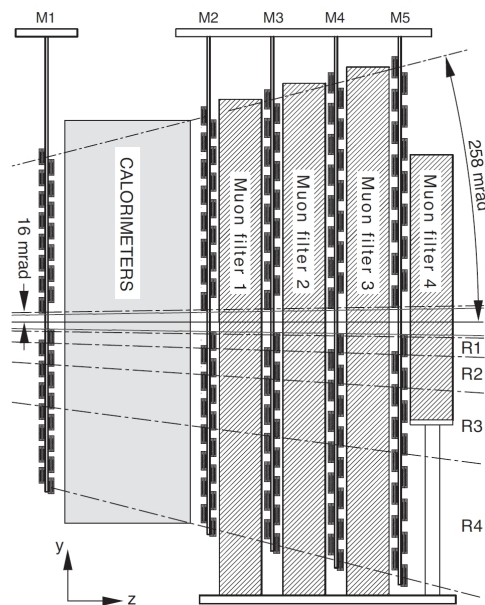


Figure 3.8: The Muon System in the $y - z$ plane. The chambers (rectangles in dark-grey) sizes vary from 0.1m² (region R1) to 0.5m² (region R4).

The muon track reconstruction is made as follow: When a hit is found in M3, hits are also searched in M2, M4 and M5. In the case that a hit is found

in the four stations (M2 - M5), the hits in M2 and M3 are used to extrapolate a point in M1 (localized before the calorimeters). Then, the hit in M1 closest to the extrapolation point is selected. See Figure 3.9.

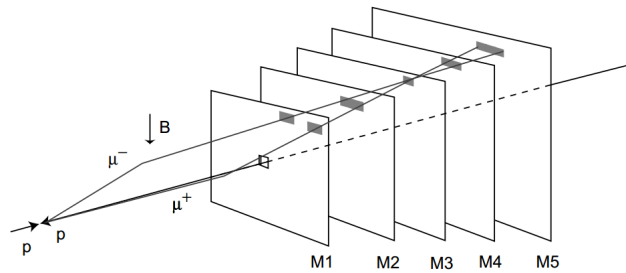


Figure 3.9: Muon Stations M1-M5. In this figure, the muons μ^+ and μ^- hit the same pad in M3.

3.3.4 The Trigger System

The beams of protons into the LHC collide at a crossing rate of 40 MHz, which corresponds to 10 MHz of crossing with visible $p-p$ interactions at the LHCb, producing around 10 TB of data per second. Since this huge amount of data is too difficult to be read and saved in hard drives and, at the same time, the majority of this information does not represent events in which the LHCb is interested, most of the data should be dismissed before it is stored. Therefore, a system taking fast and efficient decisions over the produced events is needed. Indeed, such a system is called Trigger and filters data in real-time, reducing the rate of data writing to around 5 KHz. With these purposes in mind, the Trigger System has been divided in Level-0 Trigger (L0) and High Level Trigger (HLT).

Level-0 Trigger (L0)

This system works at a hardware level, and its primary aim is to reduce the initial ratio of data writing from 10 MHz to 1 MHz. The system selects electrons, muons, photons and hadrons with high transverse momentum and energy. Therefore, such selection is based on information collected from the muon chamber, the electromagnetic (ECAL) and hadronic calorimeters (HCAL). Then, all this information is sent to a Decision Unit (L0DU), in which the event is approved or not; such a decision should be made not longer than $4\mu\text{s}$ after the beams collide.

High Level Trigger (HLT)

Once the events have been selected by the L0 Trigger, they are now analyzed at a second level known as the High Level Trigger (HLT), which works at a software level. Then, the data is sent to the Event Filter Farm (EFF), a set of around two thousand computers running the HLT algorithms. The HLT system is also divided in two stages:

- **HLT1:** Its main goal is to reduce the events rate to 10 KHz. A partial reconstruction of events is made by using information from the VELO system and the track stations. Furthermore, cuts on these (reconstructed) events such as momentum and impact parameters are applied.
- **HLT2:** Its main goal is to reduce the events rate to 5 KHz. For this reason, fast reconstruction algorithms are applied on the data selected by HLT1. Due to a total reconstruction of events made at this stage, exclusive and inclusive processes mainly of hadrons b and c can be selected. Indeed, these selections are separated in *strings* representing a specific kind of decay, e.g. a string from HLT2, such a H1t2CharmHadD2HHH, represents a charm decay into three hadrons.

Trajectory System	Vertex LOcator (VELO)
	Tracking System
Track Reconstruction	The Magnet
	VELO Track
	UpStream Track
	DownStream Track
	Large Track
Particle Identification	T Track
	RICH System
	Calorimeters System
Trigger System	Muon System
	Level-0 Trigger (L0T)
	High Level Trigger (HLT)

Table 3.1: Summary of the different systems involved in the LHCb Experiment.

4

Data Selection

The LHCb experiment obtained data during Run I (2010-2012). In this dissertation, the data used for our main decay and control channels corresponds to data collected in 2012 corresponding to an integrated luminosity of 2.0 fb^{-1} and a center-of-mass energy of $\sqrt{s} = 8 \text{ TeV}$ [39] for proton-proton collisions. The information provided by the LHCb detectors is combined to reconstruct events. Most of the events, however, are not of our interest. Therefore, some criteria are necessary to enrich the data sample with events containing true $D_s^+ \rightarrow K^- K^+ K^+$ decays.

In this chapter, we present the steps and selection criteria used to get our final samples. Furthermore, fits on the invariant-mass for our main decay, $D_s^+ \rightarrow K^- K^+ K^+$, and two control channels, $D^+ \rightarrow K^- \pi^+ \pi^+$ and $D_s^+ \rightarrow K^- K^+ \pi^+$, are performed with the purpose to define the signal window in each channel.

4.1

Trigger Selection

The data collected in the LHCb experiment is initially filtered by the L0 and HLT trigger levels (see Chapter 3, 3.3.4) by different selection criteria known as trigger lines. At this stage the data selection occurs ‘on-line’. The events can be labeled of TOS (Trigger On Signal) if they are triggered by associating the information of the detector and the candidate signal itself or TIS (Trigger Independent of Signal) if they are triggered without the requirement to be associated to the candidate signal.

At the L0 level, one of the candidate tracks for the decay channels studied is required to be selected by the trigger line `D_L0HadronDecision_TOS`. Also, a combination of TIS lines were used (see Table 4.1) to consider events triggered by other part of the event.

The reconstruction of tracks is performed at the HLT1 level with a three-dimensional pattern recognition using the information provided by the VELO detector and the tracking systems OT and IT. Furthermore, since the mesons we are working with, D^+ and D_s^+ , have different lifetime and therefore all its daughter particles have a wide range of transversal momenta, all events activating this track trigger (HLT1Track) are included with the line `D_Hlt1TrackAllL0Decision_TOS`, ensuring in this way that the hadrons, muons or electrons in the tracks are not discarded. Finally, the events corre-

sponding to a charm decays in three hadrons are obtained requiring the line `D_Hlt2ChamHadD2HHHDecision_TOS` in the HLT2 trigger which uses the full event information and is an exclusive line designed for D decays to charged hadrons. Table 4.1 shows the trigger criteria performed to select the events for the three channels studied in this dissertation.

Trigger Stage	Cuts
L0	D_LOHadronDecision_TOS==1 OR D_LOHadronDecision_TIS==1 OR D_LOMuonDecision_TIS==1 OR D_LOElectronDecision_TIS==1 OR D_LOPhotonDecision_TIS==1
HLT1	D_Hlt1TrackAllL0Decision_TOS==1
HLT2	D_Hlt2CharmHadD2HHHDecision_TOS==1

Table 4.1: Trigger criteria. The selection in L0 include TOS and TIS candidates combined in logical OR. Stages HLT1 and HLT2 require events with specific TOS lines.

4.2 Stripping Selection

The data collected is further selected in an ‘off-line’ mode in order to get rid of those events that can be identified as background and improve the signal significance. The first stage of off-line selection centrally produced and known as stripping selection [40], which represent the data that will be permanently saved in the LHCb.

Among the basic criteria for event selection at this stage are the quality of tracks, good definition of vertices and an excellent identification of particles. The relevant variables are briefly described in Appendix B. In Run I (2012), the stripping cuts for selection of the LHCb data is called as `Stripping20` and for our main decay, $D_s^+ \rightarrow K^- K^+ K^+$, it defined by a line called `StrippingDshhh_KKKLine`. The full description of the stripping criteria is also given in Appendix B (Table B.1).

Figure 4.1 shows the mass spectrum for D_s^+ candidates decaying in three kaons, $M(K^- K^+ K^+)$, after the trigger and stripping selections are applied. This is the data sample from which the study presented in this dissertation begins. Additional selection criteria are, however, necessary as discussed in the following section.

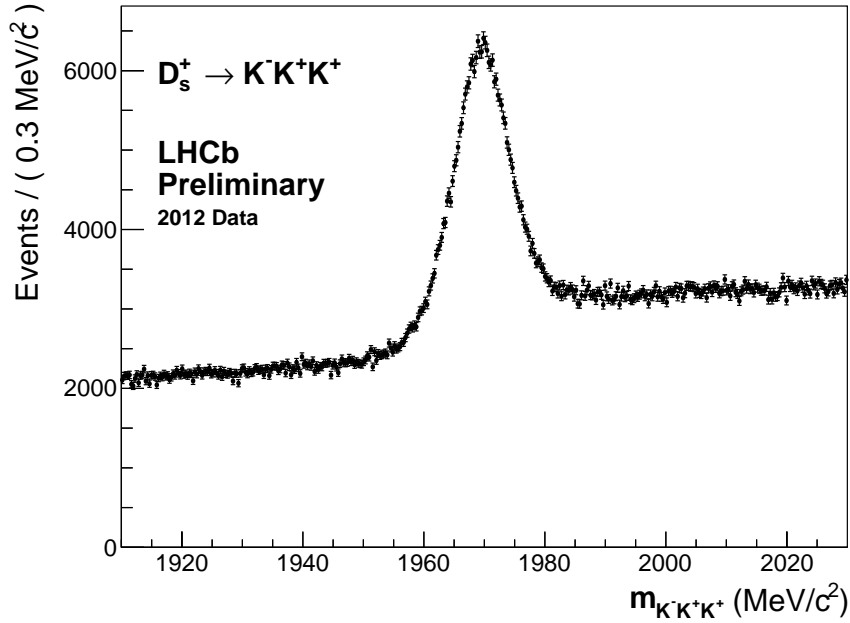


Figure 4.1: Mass spectrum for $D_s^+ \rightarrow K^- K^+ K^+$ after stripping and trigger cuts. The invariant-mass $M(K^- K^+ K^+)$ range is taken from 1910 to 2030 MeV/c^2 .

4.3 Study of Additional Selection Criteria

Since we are interested in charm meson decays in three kaons, the invariant-mass corresponding to the mother particle is calculated based on momenta and masses associated to three possible daughters. From Figure 4.1, we can observe that the peak around 1970 MeV must be formed by candidates corresponding to the expected $D_s^+ \rightarrow K^- K^+ K^+$ decay. Other candidates are from the background, both under the peak and in the mass sidebands. These can come from random three-track associations (combinatorial background) or from other D decays (reflection). Also, we should point out that the data we are working with has been taken with a given magnet orientation or polarity, namely MagUp and MagDown, which may bring systematic asymmetries in the detection/production of events. Furthermore, we analyze the data combining events with both polarities.

Therefore, we are going to apply additional cuts in our sample for the main decay, reducing the background while keeping a significant statistics for the signal. Also from Figure 4.1, we can notice that our sample shows different behaviors for the right and the left mass sidebands. The right sideband clearly has more background. The source of this is identified to be the reflection from

the decay $D^+ \rightarrow K^- K^+ \pi^+$. From a misidentification of the π^+ as a K^+ , the reconstructed mass of the D^+ shifts upwards, starting around the D_s^+ mass region. These are then $D^+ \rightarrow K^- K^+ \pi^+$ events reconstructed as $K^- K^+ K^+$.

Since $D^+ \rightarrow K^- K^+ \pi^+$ is also a Cabibbo-suppressed channel, this reflection can be potentially dangerous for our main decay. The misidentification of a π^+ can occur in any of the two K^+ in the final state. Here, we call particle 1 to the one with opposite charge with respect to the D_s^+ mother particle, then the particles labeled as 2 and 3 are the K^+ candidates. In order to suppress the $D^+ \rightarrow K^- K^+ \pi^+$ reflection, we need to apply strict particle identification selection for particles 2 and 3.

The PIDK variable indicates how likely it is for a given particle to be a kaon and, from the stripping selection, this variable started in 7 for all three kaons (see Appendix B). In Figure 4.2, we project our candidates as $M(K^- \pi^+ K^+)$ and $M(K^- K^+ \pi^+)$, thus assigning the π^+ identity to particles 2 and 3, respectively and change the PIDK cut for different values from 7 to 30. We see that the requirement of $\text{PIDK} > 20$ for both daughters makes the $D^+ \rightarrow K^- K^+ \pi^+$ reduce to a negligible level. We then adopt this criteria for our signal.

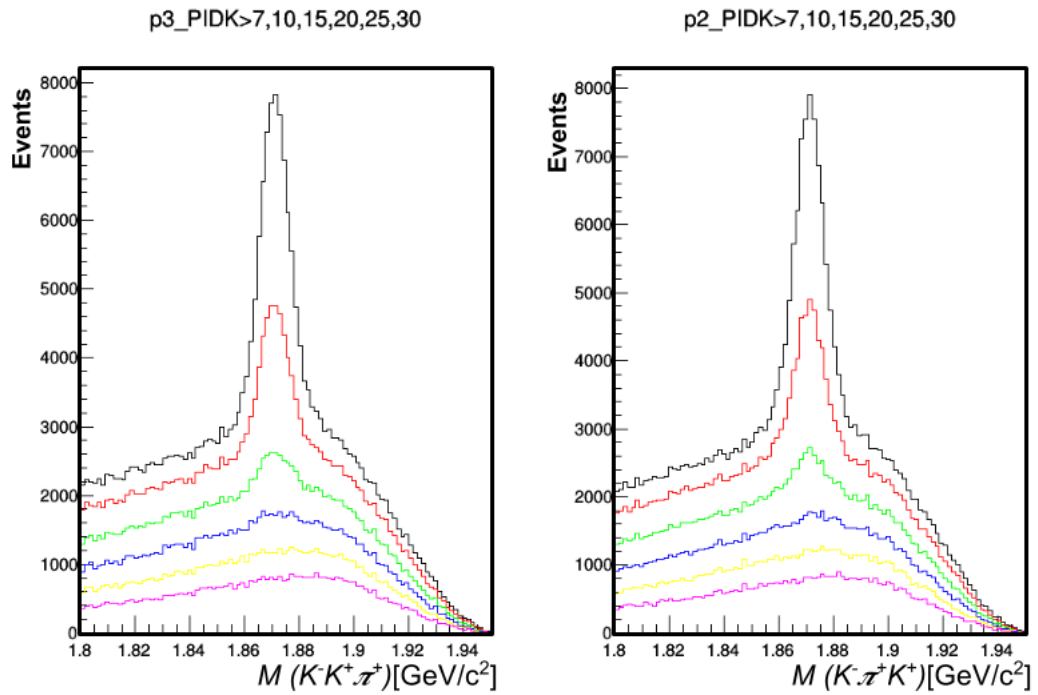


Figure 4.2: The application of PIDK cuts for the 2nd and 3rd particle. The pick is reduced when the cut on PIDK is higher. The colors for cuts in 7, 10, 15, 20, 25 and 30 are black, red, green, blue, yellow and purple, respectively. The horizontal axis in these two plots correspond to $M(K^-K^+\pi^+)$ (left) and $M(K^-\pi^+K^+)$ (right).

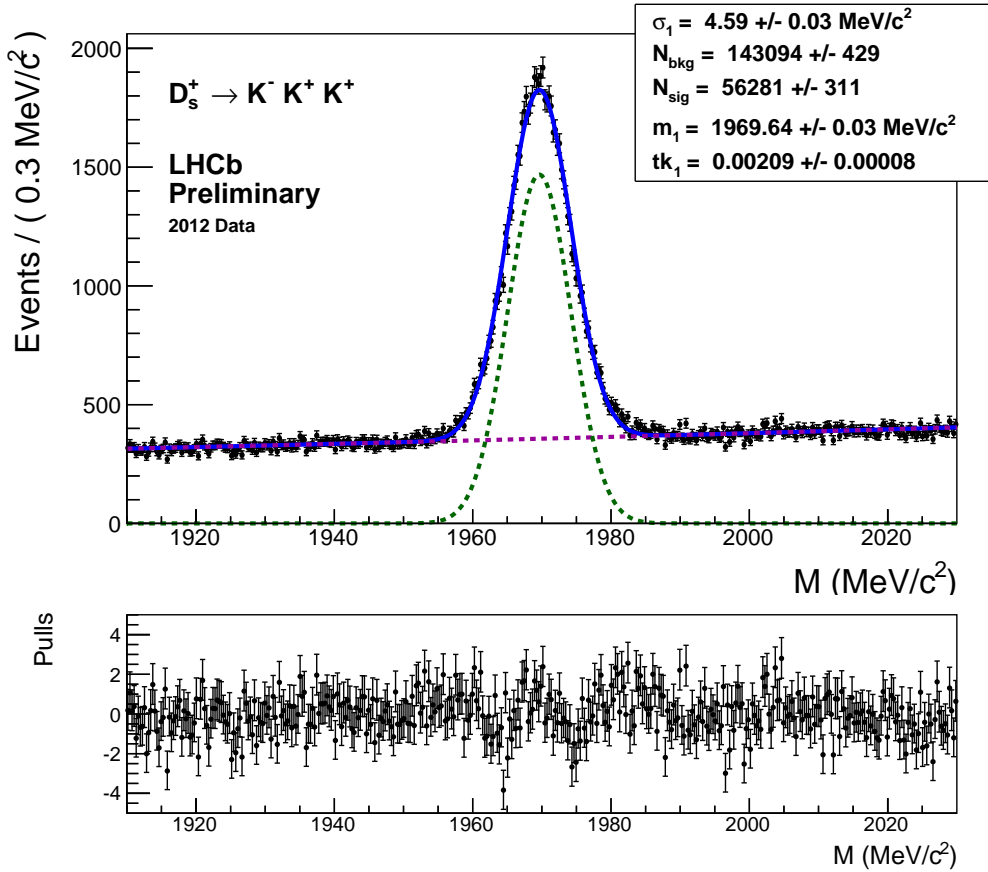


Figure 4.3: Invariant-mass distribution of $D_s^+ \rightarrow K^- K^+ K^+$ candidates after the final cuts. The total fit function (blue-line) is shown, with the signal (dashed green) and background (dashed purple) contributions.

4.4 Mass-Invariant Fits for each channel

4.4.1 $D_s^+ \rightarrow K^- K^+ K^+$ Channel

We fit our final sample with a Gaussian function to describe the $D_s^+ \rightarrow K^- K^+ K^+$ signal and an exponential for the background. The resulting fit can be seen in Figure 4.3 with a total number of signal candidates of $56,281 \pm 311$. This fit also allows to establish the signal region defined by $m \pm 2\sigma$, that is, $1960.46 < M(K^- K^+ K^+) < 1978.82 \text{ MeV}/c^2$, which will be the sample used for the CPV search in Chapter 5. Within the signal region there are 53K events with a purity of 70%, 22K events corresponding to background. The mass sidebands for our main decay are set as in Table 4.2.

Region	$M(K^-K^+K^+)$ MeV/c ²
Signal	1960.46 – 1978.82
Mass Sidebands	1932.92 – 1951.28
	1997.18 – 2015.54

Table 4.2: Signal and sidebands mass regions used for the CPV studies.

4.4.2

Control Channel 1: $D^+ \rightarrow K^- \pi^+ \pi^+$

This channel is a Cabibbo-favored decay, thus no effects of CP violation are expected. Therefore, it is used to make sure that neither local production nor detection asymmetries are present. In addition, given its very high statistics, we select just a part of it with a sample size about three times our signal sample. Since a single Gaussian fit is not enough, we use a two-gaussian fit for the invariant-mass distribution of $M(K^- \pi^+ \pi^+)$ in $D^+ \rightarrow K^- \pi^+ \pi^+$ as shown in Figure 4.4. In this case, there are five parameters describing the shape of the resulting two Gaussians: the widths σ_1 and σ_2 , means m_1 and m_2 and their relative weight f_1 and $(1 - f_1)$, respectively (see Table 4.3).

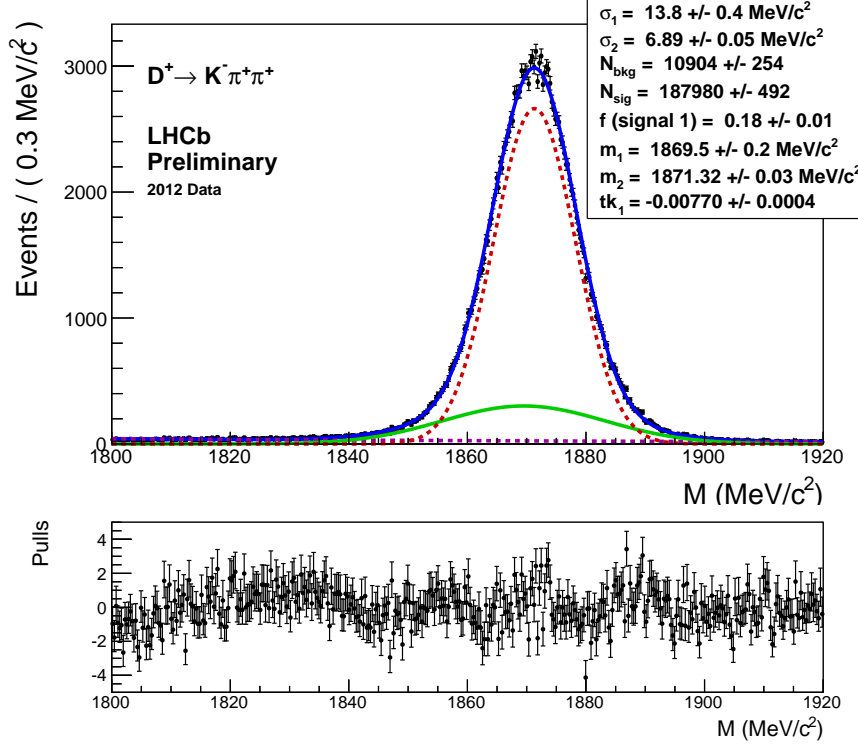


Figure 4.4: Invariant-mass distribution of $D^+ \rightarrow K^- \pi^+ \pi^+$ candidates. The total fit function (blue-line) is shown, with signal (solid green and dashed red) and background (dashed purple) contributions.

σ_1	$6.89 \pm 0.05 \text{ MeV}/c^2$
σ_2	$13.7 \pm 0.4 \text{ MeV}/c^2$
m_1	$1871.32 \pm 0.03 \text{ MeV}/c^2$
m_2	$1869.5 \pm 0.2 \text{ MeV}/c^2$
f_1	0.81 ± 0.01

Table 4.3: Result of fitting the sample for $D^+ \rightarrow K^- \pi^+ \pi^+$.

For this channel, its signal region is defined as $\tilde{m}_D \pm 2\tilde{\sigma}$, where $\tilde{\sigma}$ and \tilde{m}_D are the weighted average of the two fitted Gaussian widths and mean values.

$$\tilde{\sigma} = \sqrt{f_1 \cdot \sigma_1^2 + (1 - f_1) \cdot \sigma_2^2} = 8.60 \quad (4.1)$$

$$\tilde{m}_D = f_1 \cdot m_1 + (1 - f_1) \cdot m_2 = 1870.97 \quad (4.2)$$

The signal region for this channel is thus $1853 < M(K^- \pi^+ \pi^+) < 1888.17 \text{ MeV}/c^2$.

4.4.3

Control Channel 2: $D_s^+ \rightarrow K^- K^+ \pi^+$

As in the previous control channel, no CP violation is expected since it is a Cabibbo-favored decay and share the same mother particle as our main decay. Thus, it is also important to check for a possible presence of nuisance asymmetries. We proceed by fitting the invariant mass $M(K^- K^+ \pi^+)$ for D_s^+ candidates using a sample of around one million events and requiring for the second particle to have the same PDIDK>20 cut as in our main decay. The fit is performed using two Gaussian functions for signal and exponential for the background. The resulting fit is shown in Figure 4.5.

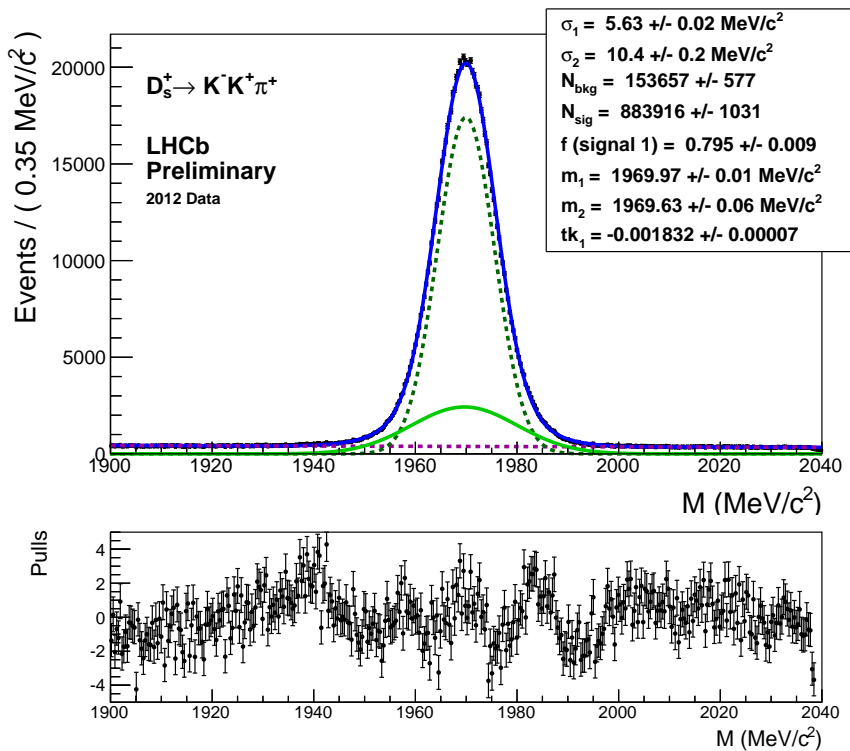


Figure 4.5: Invariant-mass distribution of $D_s^+ \rightarrow K^- K^+ \pi^+$ candidates. The total fit function (blue-line) is shown, with signal (solid and dashed green) and background (dashed purple) contributions

From the fit we can obtain a standard deviation of $\tilde{\sigma} = 6.88 \text{ MeV}/c^2$ and a mass mean of $\tilde{m} = 1969.87 \text{ MeV}/c^2$, see Table 4.4. The signal region for this channel is defined as $\tilde{m} \pm 2\sigma$, that is $1969.90 \pm 13.76 \text{ MeV}/c^2$.

σ_1	$5.63 \pm 0.02 \text{ MeV}/c^2$
σ_2	$10.4 \pm 0.2 \text{ MeV}/c^2$
m_1	$1969.97 \pm 0.01 \text{ MeV}/c^2$
m_2	$1969.63 \pm 0.06 \text{ MeV}/c^2$
f_1	0.795 ± 0.009

Table 4.4: $M(K^-K^+\pi^+)$ fit data.

5

Search for CP Violation in $D_s^+ \rightarrow K^- K^+ K^+$ Decays at LHCb

In this chapter, we focus on the search for CP violation in the phase space of the decay $D_s^+ \rightarrow K^- K^+ K^+$ using proton-proton collision data that was collected by the LHCb experiment in 2012. One way to search for direct CP violation could be made by calculating the difference between time-integrated decay rates for D_s^+ and D_s^- , which is the approach for two-body decays. However, this single number may not be enough to understand the mechanisms leading to CPV asymmetry, if found.

Therefore, we are going to look for localized asymmetries in the Dalitz plot distribution for D_s^+ and D_s^- candidates through a model-independent technique known as the Mirandizing Method [41]. The signal region of our decay of interest is going to be analyzed by this method, only after we are confident that nuisance local asymmetries are not affecting our results. Two control channels $D_s^+ \rightarrow K^- K^+ \pi^+$ and $D^+ \rightarrow K^- \pi^+ \pi^+$ are used to ensure that these kind of asymmetries are not present. These channels are chosen because no CP violation is expected for them. We also investigate the mass sidebands consisting of background of our signal.

5.1

Mirandizing Method

In this method, the Dalitz plots of D_s^+ and D_s^- are split into bins and a CP significance variable S_{CP}^i [42] is defined in order to search for localized asymmetries,

$$S_{CP}^i = \frac{N_i^+ - \alpha N_i^-}{\sqrt{\alpha(N_i^+ + N_i^-)}}, \quad \alpha = \frac{N^+}{N^-}, \quad (5.1)$$

where N_i^+ (N_i^-) is the number of D_s^+ (D_s^-) candidates in the i th bin and N^+ (N^-) is the sum of N_i^+ (N_i^-) over all bins. The parameter α is introduced to remove the contribution from charge asymmetries that do not vary across the Dalitz plots, an *a priori* global asymmetry that may be due to production effects, detection efficiency or also a global CPV. Therefore, this normalization would not allow us to be sensitive to a CPV that is constant on a Dalitz plot. Nevertheless, this last scenario is unlikely because of the presence of two-particle resonances.

If no localized asymmetries are present across the Dalitz plots, the values of S_{CP}^i must follow a standard normal Gaussian distribution, thus, a variation from this behavior would evidence the presence of CPV asymmetry. Furthermore, a χ^2 test is used to perform a numerical comparison between the

bins of the D_s^+ and D_s^- Dalitz plots, where $\chi^2 = \sum_i (S_{CP}^i)^2$ [43]. The number of degrees of freedom (ndf) equals the total number of bins minus one, due to the constraint made when introducing α for the normalization over D_s^+ and D_s^- . A p-value is obtained from this test, defined as the probability of obtaining a χ^2 that is at least as high as the value observed, given a ndf and under the assumption of no CPV (null hypothesis). It gives us the confidence that the any difference between the Dalitz plots is only due to statistical fluctuations.

The Mirandizing Method is applied by using two types of binning: A **uniform** distribution of bins of the same size and an **adaptive** binning in which all bins contain almost the same number of events. The last approach is useful when there is an important non-uniform event distribution, due to the presence of resonances in the Dalitz plot.

5.2

Control Mode 1: $D^+ \rightarrow K^- \pi^+ \pi^+$ Decay

Since this channel is a Cabibbo-favored decay, no effects of CP violation are expected. Therefore, it is used to make sure that neither local production nor detection asymmetries are present. We are going to apply the Mirandizing method in its signal region that corresponds to events in the range of $\tilde{m}_D \pm 2\tilde{\sigma}$, that is, a signal window where the invariant-mass is between $1853.77 < M(K^- \pi^+ \pi^+) < 1888.17$ MeV/c² as discussed in Chapter 4. The total sample size corresponds to about 180 thousand events, which is almost three times our signal sample, so it has a higher sensitivity to eventual asymmetries. Since there are two identical pions in the final state of this decay, the Dalitz plot is ‘folded’ with respect to its diagonal by choosing as axis the variables s_{low} and s_{high} , that is, the lowest and highest invariant-mass squared combination $m^2(K^- \pi^+)$, respectively. Figure 5.1 shows the Dalitz Plot for events in the mentioned region.

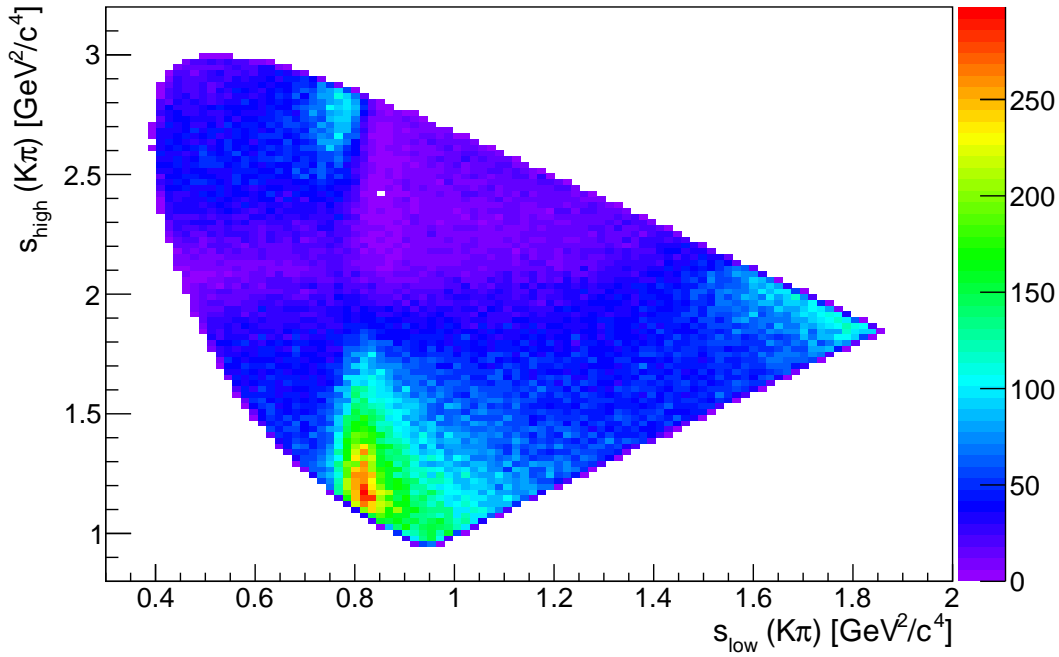


Figure 5.1: Dalitz Plot of $D^+ \rightarrow K^- \pi^+ \pi^+$ in its signal region. Total number of events: 89,264 for D^+ and 92,135 for D^- .

5.2.1 Uniform Binning

We divide the Dalitz plots in grids of 8×8 and 15×15 uniform bins. First, we divide the ranges of s_{low} and s_{high} in 8 same-width parts, obtaining in this way 64 bins with the same area. Then, we apply the Mirandizing method over the Dalitz plot of D^+ and D^- , considering bins with at least 20 events in both Dalitz plots to avoid misleading fluctuations. The number of bins meeting this last requirement is going to be called ‘ngood’. Figure 5.2(a) shows the values of S_{CP} for each bin in a range of -5 to 5 (z-axis), while Figure 5.2(b) shows the distribution of these S_{CP} values. The same is shown for the 15×15 grid in Figure 5.3. The results of these two uniform binnings, as summarized in Table 5.1, show p-values of 78.7% and 59.1%, thus compatible with normal distributions, that is, no nuisance asymmetries are present.

Binning	N^+	N^-	α	χ^2	ndf	p-value
8×8	89,252	92,123	0.968835	20.079	26	78.7%
15×15	89,206	92,084	0.968746	96.103	100	59.1%

Table 5.1: Results for uniform binning of $D^+ \rightarrow K^- \pi^+ \pi^+$ Dalitz Plot.

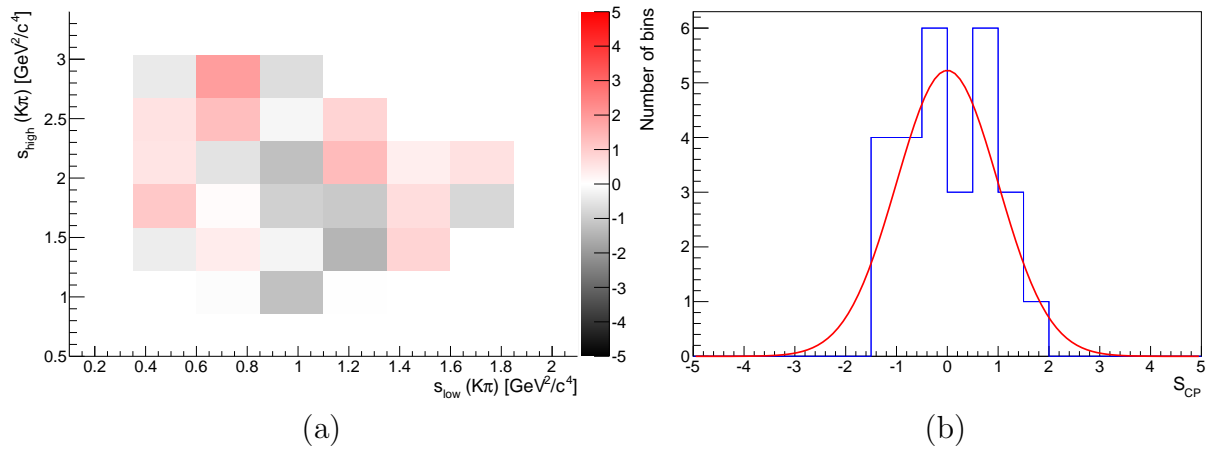


Figure 5.2: (a) Distribution of the values of S_{CP}^i with 8×8 uniform bins in the $D^+ \rightarrow K^- \pi^+ \pi^+$ Dalitz plot. (b) The corresponding one-dimensional distribution of S_{CP} with a standard normal Gaussian function superimposed (red-line).

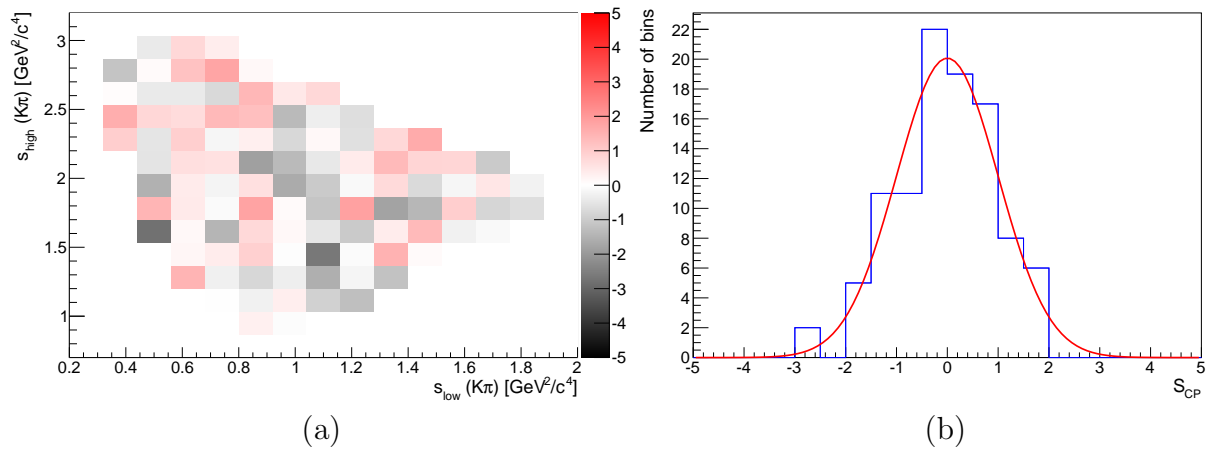


Figure 5.3: (a) Distribution of the values of S_{CP}^i with 15×15 uniform bins in the $D^+ \rightarrow K^- \pi^+ \pi^+$ Dalitz plot. (b) The corresponding one-dimensional distribution of S_{CP} with a standard normal Gaussian function superimposed (red-line).

5.2.2 Adaptive Binning

In order to get a binning with equal event population in each bin, we take one part of the data, in this case, the events for the MagUp sample. For instance, the corresponding DP for these events can be divided in 24 bins in the following way: Let N be the total number of events, we then identify a first coordinate x_1 in the x -axis for which the number of events with $s_{low} < x_1$ is $N/6$ (integer division), after that, we identify a second coordinate in x -axis, x_2 for which the number of events with $x_1 < s_{low} < x_2$ is $N/6$. The same process continues until five coordinates x_1, x_2, \dots, x_5 are found which determine 6 “vertical” regions with the same amount of events. Then, into each of these regions three y ’s (y_1, y_2, y_3) coordinates are found so that they divide each region in 4 bins with the same number of events $N/24$.

Figure 5.4 shows the resulting Dalitz Plot divided in 24 adaptive bins. The “grid” constructed in this way, that is, the total set of vertex (s_{low}, s_{high}) for all the bins is going to be used in the DPs of D^+ and D^- . After the Mirandizing method is performed for these Dalitz plots, we found that the values of S_{CP} also follows a Gaussian distribution as shown in Figure 5.5.

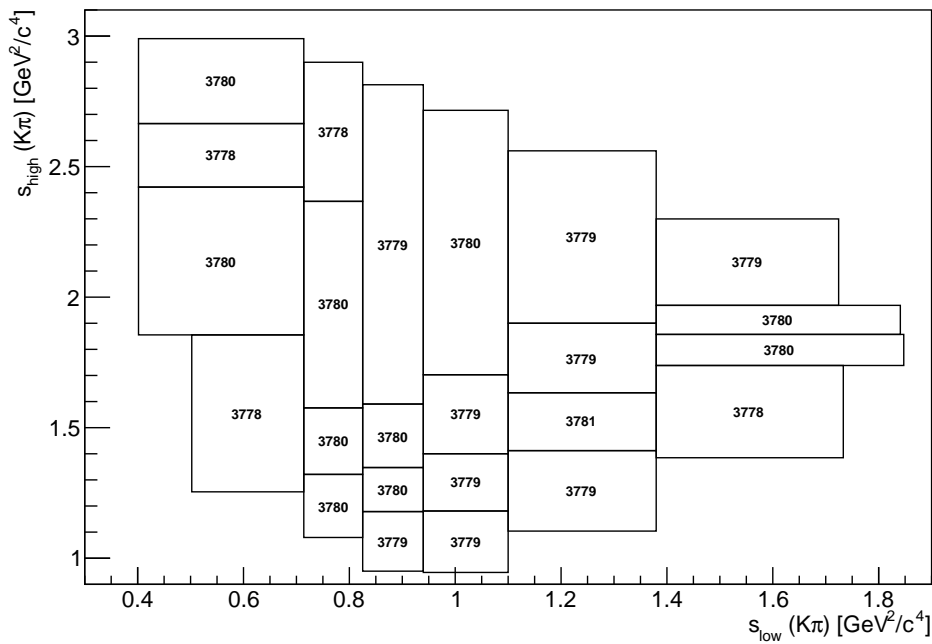


Figure 5.4: Adaptive Binning of a Dalitz Plot of $D^+ \rightarrow K^- \pi^+ \pi^+$ in 24 bins. A total of 90,710 events of MagUp sample in the region $1853.77 < M(K^- \pi^+ \pi^+) < 1888.17 \text{ MeV}/c^2$ are divided in bins with equal population (around 3,780 events per bin).

PUC-Rio - Certificação Digital N° 1322132/CA

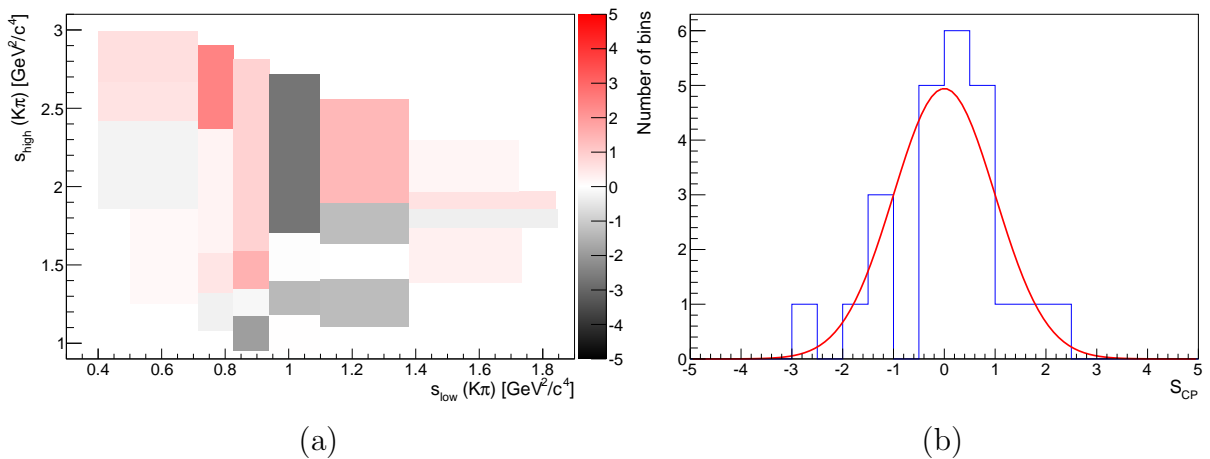


Figure 5.5: (a) Distribution of the values of S_{CP}^i with 24 adaptive bins in the $D^+ \rightarrow K^- \pi^+ \pi^+$ Dalitz plot. (b) The corresponding one-dimensional distribution of S_{CP} with a standard normal Gaussian function superimposed (red-line).

We also perform two additional binnings to obtain a better resolution of possible local asymmetries. Figures 5.6 and 5.7 show the distribution of S_{CP} for 64 and 144 adaptive binnings, respectively. We can observe that the χ^2 is close to the number of bins in each of the three binnings applied and that p-values also increment as the number of bins get higher, see Table 5.2. Indeed, the behavior of the asymmetry variable S_{CP} verifies that it follows a normal Gaussian distribution and, therefore, the absence of undesired asymmetries in this control channel.

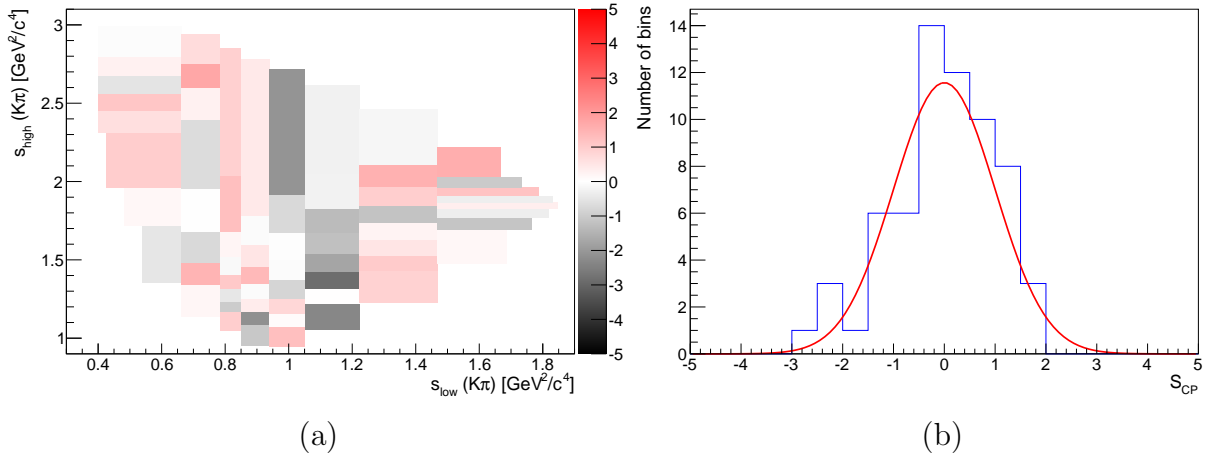


Figure 5.6: (a) Distribution of the values of S_{CP}^i with 64 adaptive bins in the $D^+ \rightarrow K^- \pi^+ \pi^+$ Dalitz plot. (b) The corresponding one-dimensional distribution of S_{CP} with a standard normal Gaussian function superimposed (red-line).

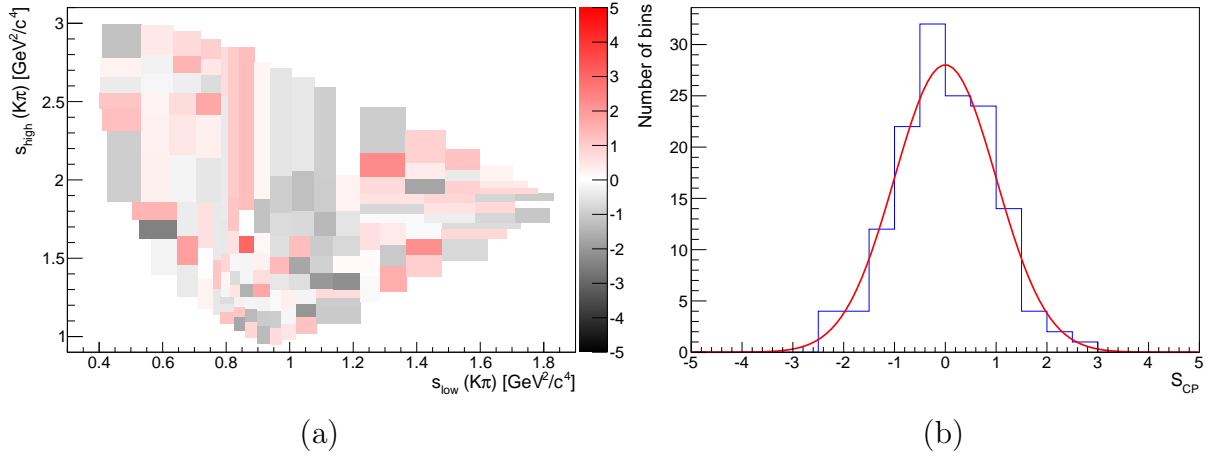


Figure 5.7: (a) Distribution of the values of S_{CP}^i with 144 adaptive bins in the $D^+ \rightarrow K^- \pi^+ \pi^+$ Dalitz plot. (b) The corresponding one-dimensional distribution of S_{CP} with a standard normal Gaussian function superimposed (red-line).

Binning	N^+	N^-	α	χ^2	p-value
24	89,252	92,123	0.968835	28.681	19.1%
64	89,251	92,121	0.968845	65.304	39.6%
144	89,237	92,099	0.968925	131.685	74.1%

Table 5.2: Results for adaptive binning of $D^+ \rightarrow K^- \pi^+ \pi^+$ Dalitz plot. Total positives 89,264 and negatives 92,135. $\text{ndf} = \text{Binning} - 1$.

5.3

Control Channel 2: $D_s^+ \rightarrow K^- K^+ \pi^+$

As in the previous channel, the Mirandizing method is applied on uniform and adaptive binnings for the signal window of this decay, that is, $1956.14 < M(K^- K^+ \pi^+) < 1983.66$ MeV. In this region, 433,865 (436,092) events correspond to the decay of D_s^+ (D_s^-). One feature of this decay is that it shares the same mother particle (D_s) as our main decay. Figure 5.8 shows the Dalitz plot for $D_s^+ \rightarrow K^- K^+ \pi^+$, where the z-axis is expressed in logarithmic scale to appreciate the non-uniform distribution of events.

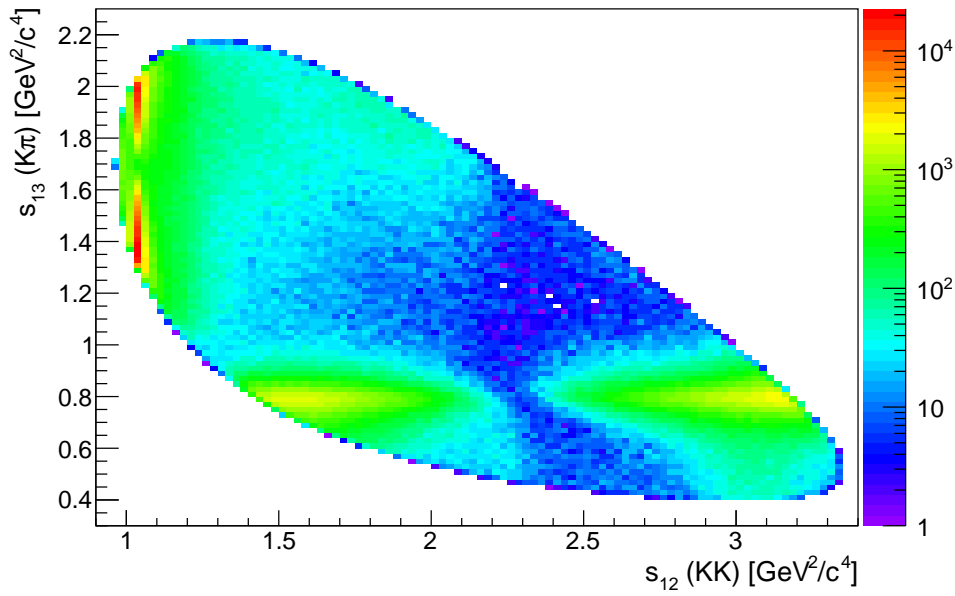


Figure 5.8: The Dalitz Plot of $D_s^+ \rightarrow K^- K^+ \pi^+$. The plot has been expressed in logarithmic scale to show the non-uniform distribution of events.

5.3.1

Uniform Binning

The Mirandizing method is applied on two uniform binnings of the Dalitz plot of $D_s^+ \rightarrow K^- K^+ \pi^+$, 8×8 and 15×15 . The former binning has $\alpha = 0.994734$, a $\chi^2 = 25.808$, a p-value of 58.3%. Compatible results are obtained for the later 15×15 binning, see Figure 5.9.

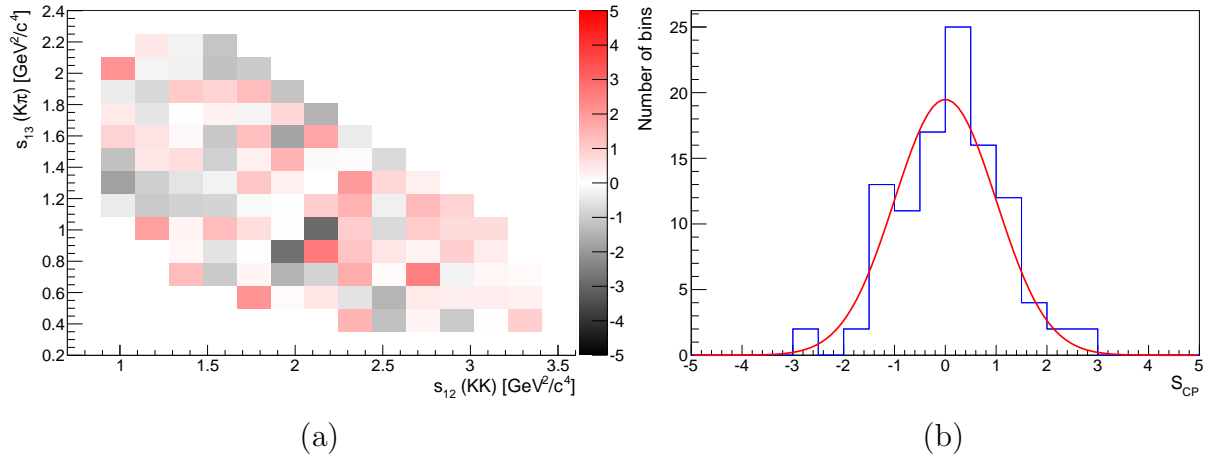


Figure 5.9: (a) Distribution of the values of S_{CP}^i with 15×15 uniform bins in the $D_s^+ \rightarrow K^- K^+ \pi^+$ Dalitz plot. (b) The corresponding one-dimensional distribution of S_{CP} with a standard normal Gaussian function superimposed (red-line).

Table 5.3 summarizes the results for these two uniform binnings and confirms that the asymmetry variable S_{CP} follows a normal Gaussian distribution.

Binning	N^+	N^-	α	χ^2	ndf	p-value
8×8	432,181	434,469	0.994734	25.808	28	58.3%
15×15	433,854	436,089	0.994875	115.639	105	22.4%

Table 5.3: Results for uniform binning of $D_s^+ \rightarrow K^- K^+ \pi^+$ Dalitz plot.

5.3.2 Adaptive Binning

For the present channel, we took a sample of around 850 thousand events, about 11 times our sample signal. Thus again we test for eventual asymmetries with higher sensitivity. Figure 5.10 shows the distribution of the asymmetry variable over the Dalitz plot of $D_s^+ \rightarrow K^- K^+ \pi^+$ for 24 adaptive bins, where α is 0.994949, χ^2 equals 29.960 and a p-value of 15.0%. Figures 5.11 and 5.12 show the distribution of S_{CP}^i for 64 and 144 adaptive binnings, respectively. The results for these adaptive binnings are summarized in Table 5.4, they validate the null hypothesis, that is, no unexpected asymmetries this control channel.

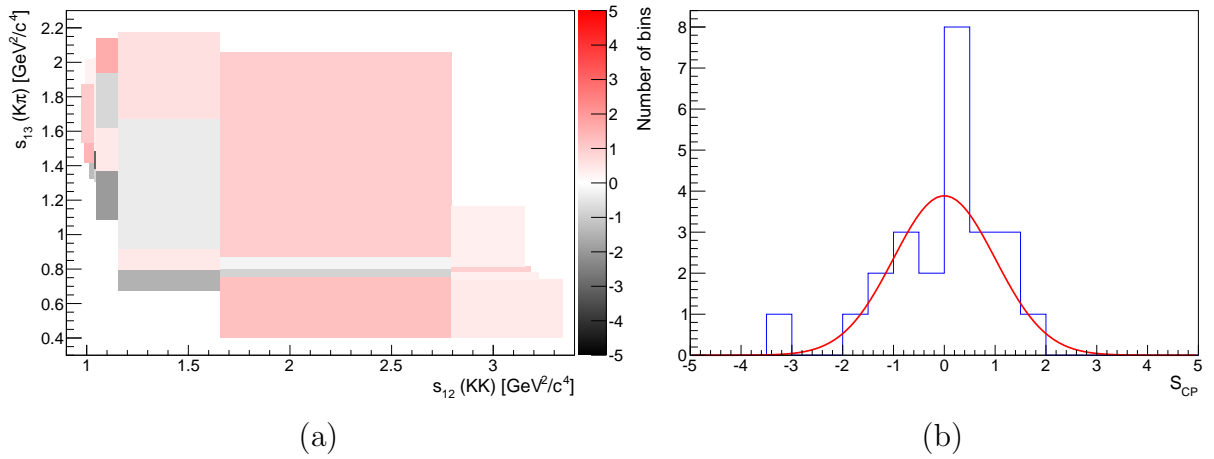


Figure 5.10: (a) Distribution of the values of S_{CP}^i with 24 adaptive bins in the $D_s^+ \rightarrow K^- K^+ \pi^+$ Dalitz plot. (b) The corresponding one-dimensional distribution of S_{CP} with a standard normal Gaussian function superimposed (red-line).

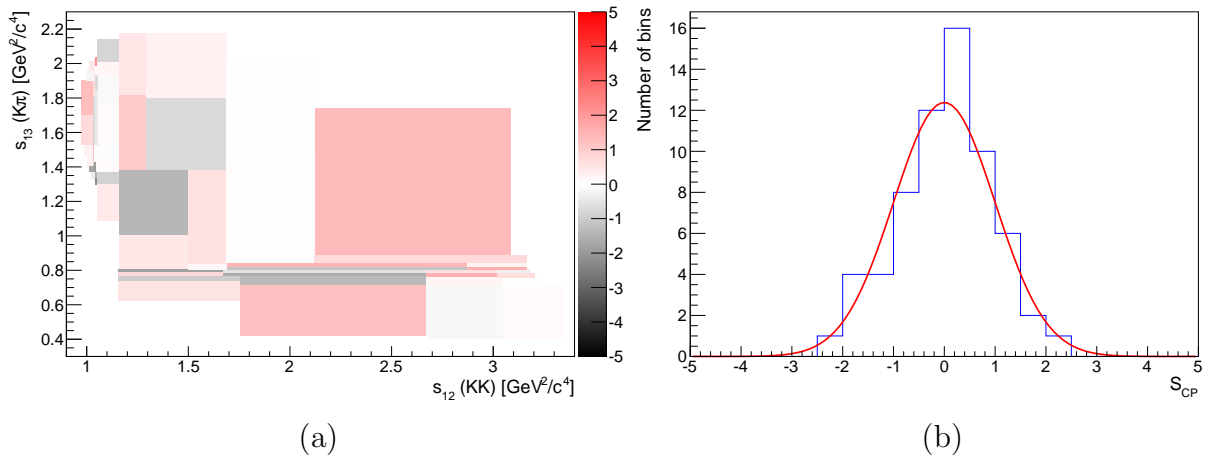


Figure 5.11: (a) Distribution of the values of S_{CP}^i with 64 adaptive bins in the $D_s^+ \rightarrow K^- K^+ \pi^+$ Dalitz plot. (b) The corresponding one-dimensional distribution of S_{CP} with a standard normal Gaussian function superimposed (red-line).

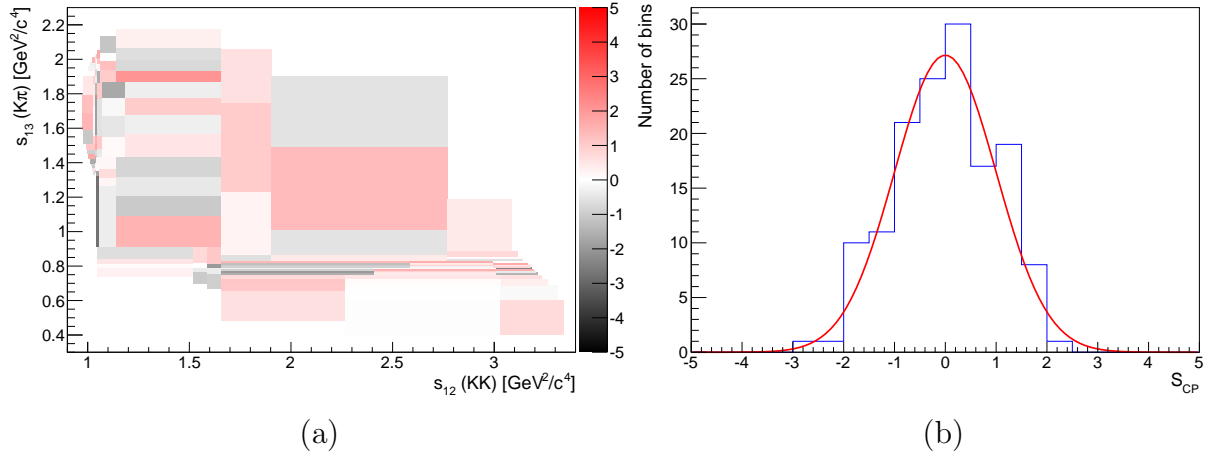


Figure 5.12: (a) Distribution of the values of S_{CP}^i with 144 adaptive bins in the $D_s^+ \rightarrow K^- K^+ \pi^+$ Dalitz plot. (b) The corresponding one-dimensional distribution of S_{CP} with a standard normal Gaussian function superimposed (red-line).

Binning	N^+	N^-	α	χ^2	p-value
24	434,126	436,330	0.994949	29.960	15.0%
64	434,118	436,331	0.994928	55.354	74.2%
144	434,118	436,321	0.994951	139.096	57.6%

Table 5.4: Results for adaptive binning of $D_s^+ \rightarrow K^- K^+ \pi^+$ Dalitz plot. ndf = Binning - 1.

5.4

Background: Mass Sidebands of $K^- K^+ K^+$

The signal region, besides true $D_s^+ \rightarrow K^- K^+ K^+$ decays, also has 29.7% of background contribution (see Section 4.4.1). It is important to check whether the background introduce asymmetries. For this purpose, we study the mass sidebands within 1932.92 - 1951.28 MeV/ c^2 and 1997.18 - 20015.54 MeV/ c^2 (see Table 4.2). As for the control channels, we apply the Mirandizing method for different choices of uniform and adaptive binnings.

5.4.1

Uniform Binning

Figure 5.13 shows the Dalitz plot in the present region. Again, we use two different uniform binnings for the Dalitz plots, 8×8 and 15×15 . The results of applying the Mirandizing method, using the former uniform binning, are

$\alpha = 1.05837$, $\chi^2 = 16.889$ and a p-value of 91.2%. Figures 5.14 and 5.15 show the S_{CP} distribution for the two binnings whose results are found in Table 5.5, which strongly suggests the absence of CPV for this region.

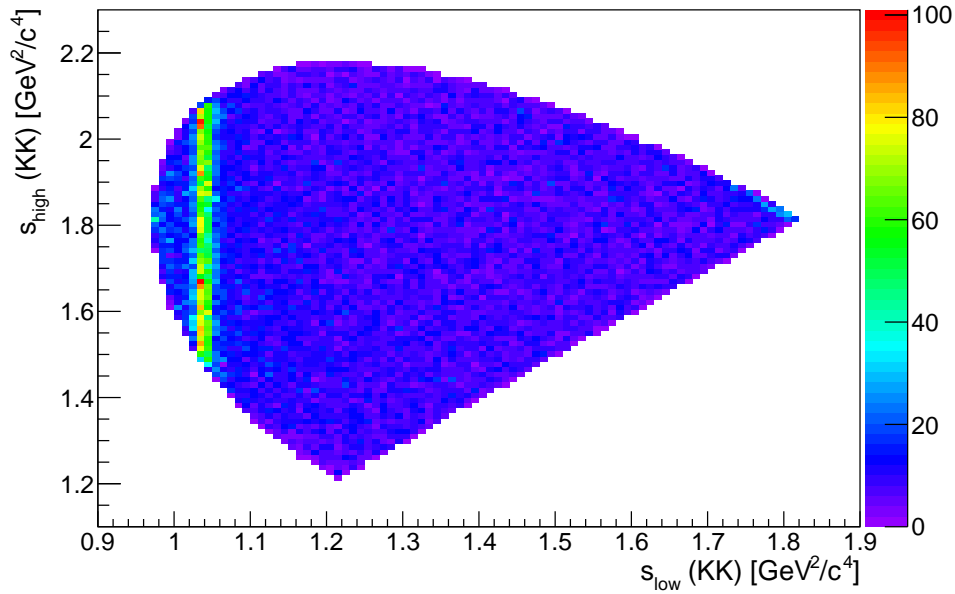


Figure 5.13: Dalitz Plot of $D_s^+ \rightarrow K^- K^+ K^+$ in its background region.

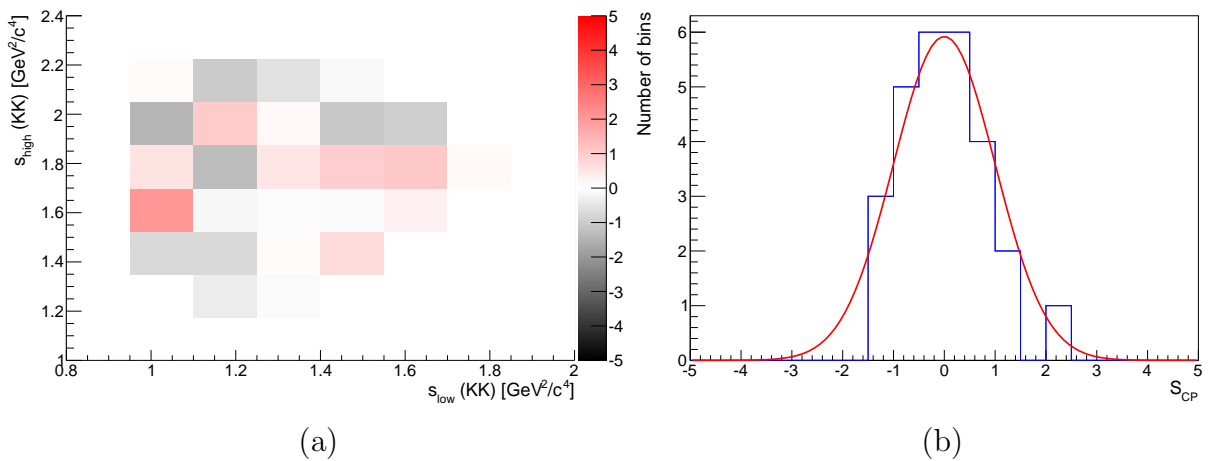


Figure 5.14: (a) Distribution of the values of S_{CP}^i with 8×8 uniform bins in the Dalitz plot of the mass sidebands of $K^- K^+ K^+$. (b) The corresponding one-dimensional distribution of S_{CP} with a standard normal Gaussian function superimposed (red-line).

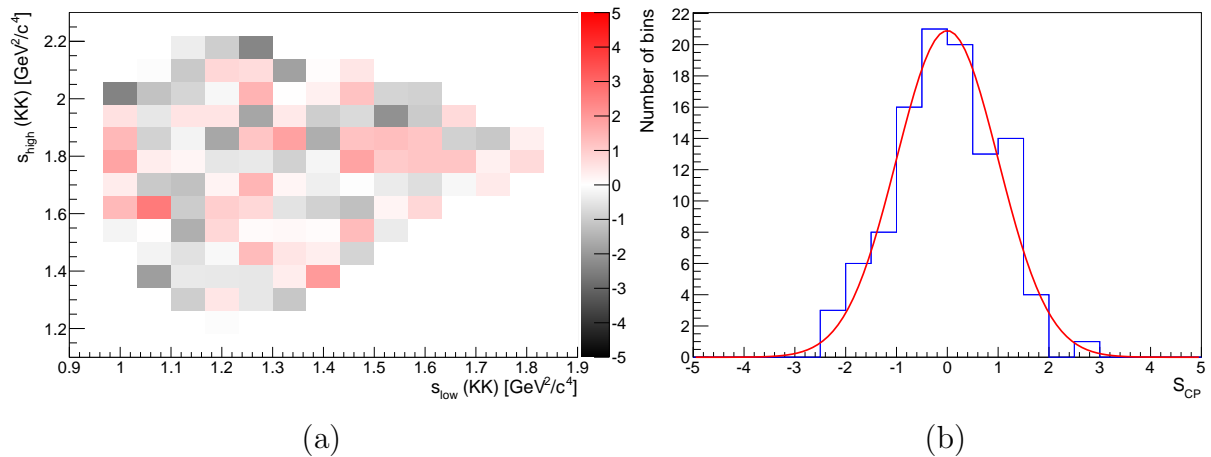


Figure 5.15: (a) Distribution of the values of S_{CP}^i with 15×15 uniform bins in the Dalitz plot of the mass sidebands of $K^- K^+ K^+$. (b) The corresponding one-dimensional distribution of S_{CP} with a standard normal Gaussian function superimposed (red-line).

Binning	N^+	N^-	α	χ^2	ndf	p-value
8×8	22,519	21,277	1.05837	16.889	26	91.2%
15×15	22,422	21,211	1.05709	108.059	105	39.9%

Table 5.5: Results for uniform binning of the Dalitz Plot of mass sidebands of $K^- K^+ K^+$.

5.4.2 Adaptive Binning

The Mirandizing method is applied on the Dalitz plot with 24, 64 and 144 adaptive bins. Figures 5.16, 5.17 and 5.18 depict the distribution of the variable S_{CP} for these adaptive binnings. Note, that this variable follows, as in the previous cases, a normal distribution. The results for the three binnings are summarized in Table 5.6.

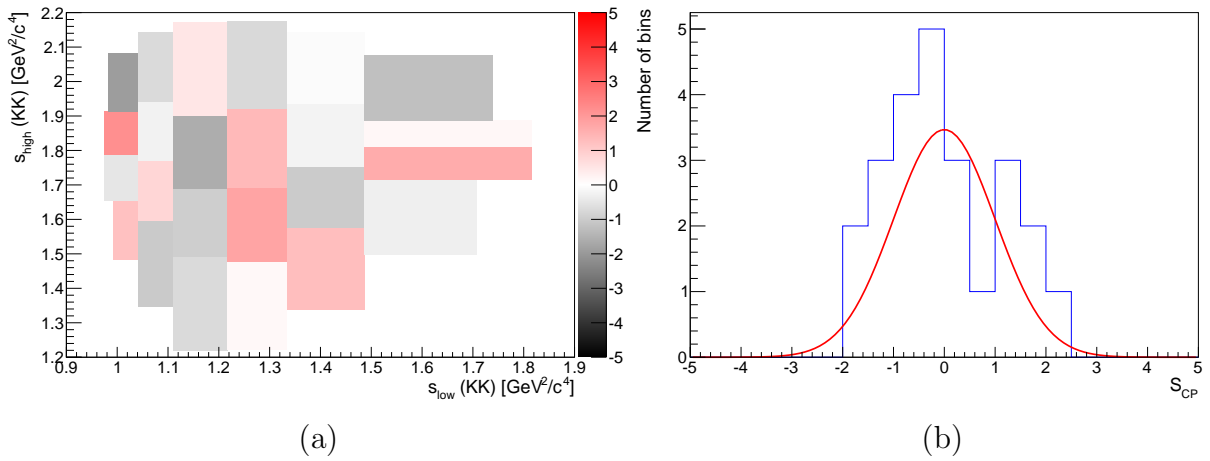


Figure 5.16: (a) Distribution of the values of S_{CP}^i with 24 adaptive bins in the Dalitz plot of the mass sidebands $K^- K^+ K^+$. (b) The corresponding one-dimensional distribution of S_{CP} with a standard normal Gaussian function superimposed (red-line).

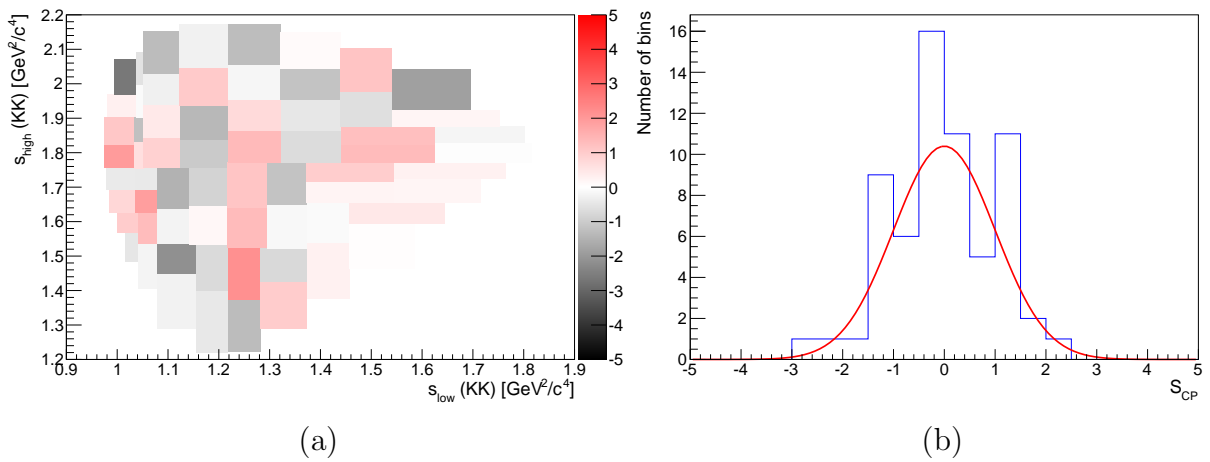


Figure 5.17: (a) Distribution of the values of S_{CP}^i with 64 adaptive bins in the Dalitz plot of the mass sidebands $K^- K^+ K^+$. (b) The corresponding one-dimensional distribution of S_{CP} with a standard normal Gaussian function superimposed (red-line).

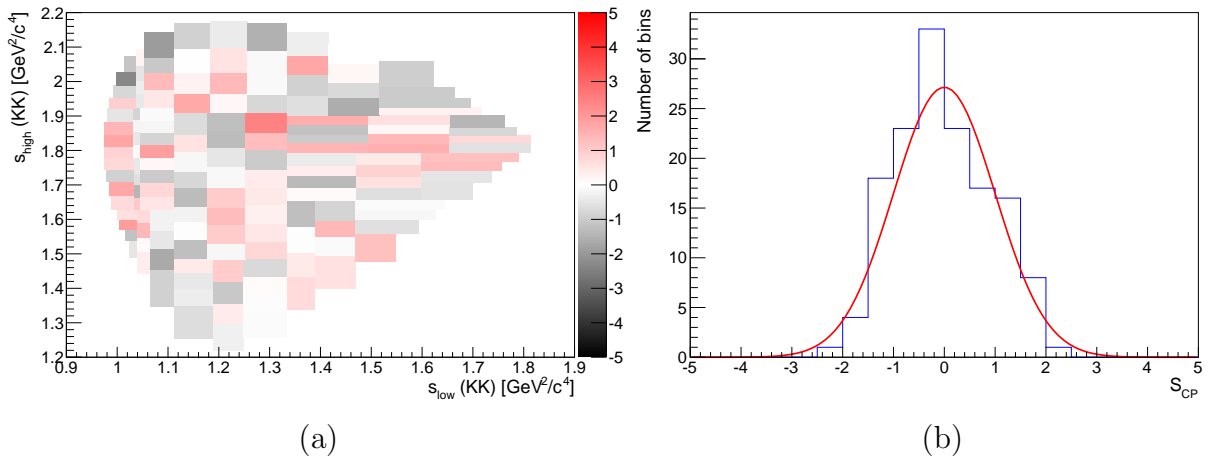


Figure 5.18: (a) Distribution of the values of S_{CP}^i with 144 adaptive bins in the Dalitz plot of the mass sidebands $K^- K^+ K^+$. (b) The corresponding one-dimensional distribution of S_{CP} with a standard normal Gaussian function superimposed (red-line).

Binning	N^+	N^-	α	χ^2	p-value
24	22,500	21,269	1.05788	29.266	17.1%
64	22,488	21,260	1.05776	65.834	37.9%
144	22,475	21,237	1.05829	125.596	84.9%

Table 5.6: Results for adaptive binning of the Dalitz plot of mass sidebands of $K^- K^+ K^+$. ndf = Binning-1.

5.5

$D_s^+ \rightarrow K^- K^+ K^+$ Signal Region

Once we have shown that there are no indications of local asymmetries induced by detection or production effects, we are ready to study the $D_s^+ \rightarrow K^- K^+ K^+$ decay. Furthermore, the signal region for this channel relies on the range of $1960.46 < M(K^- K^+ K^+) < 1978.82$ MeV/ c^2 . Figure 5.19 shows the Dalitz plot in the signal window, where there are 37,925 D_s^+ and 37,488 D_s^- candidates, where 70.3% are expected to be signal.

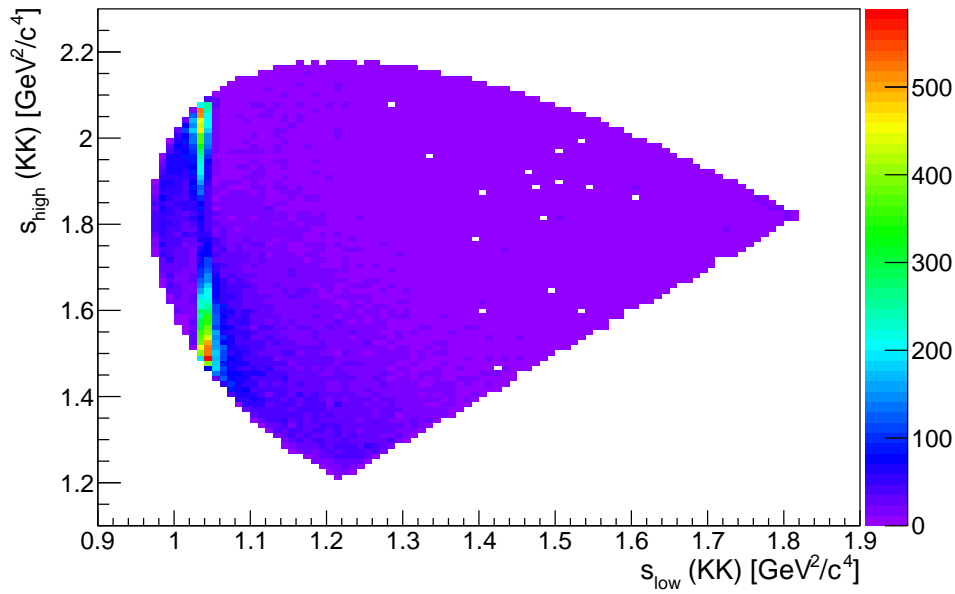


Figure 5.19: Dalitz Plot of $D_s^+ \rightarrow K^- K^+ K^+$ in its signal region. White colored bins are too small that no event is registered into them.

5.5.1

Uniform Binning

We apply the Mirandizing method in 8×8 and 15×15 binnings for the Dalitz plot in this region. The Figures 5.20 and 5.21 show that the asymmetry variable S_{CP} follows a normal distribution centered in zero. From Table 5.7 we can observe that the p-values are 72.8% and 84.4% for the grids of 8×8 and 15×15 , respectively.

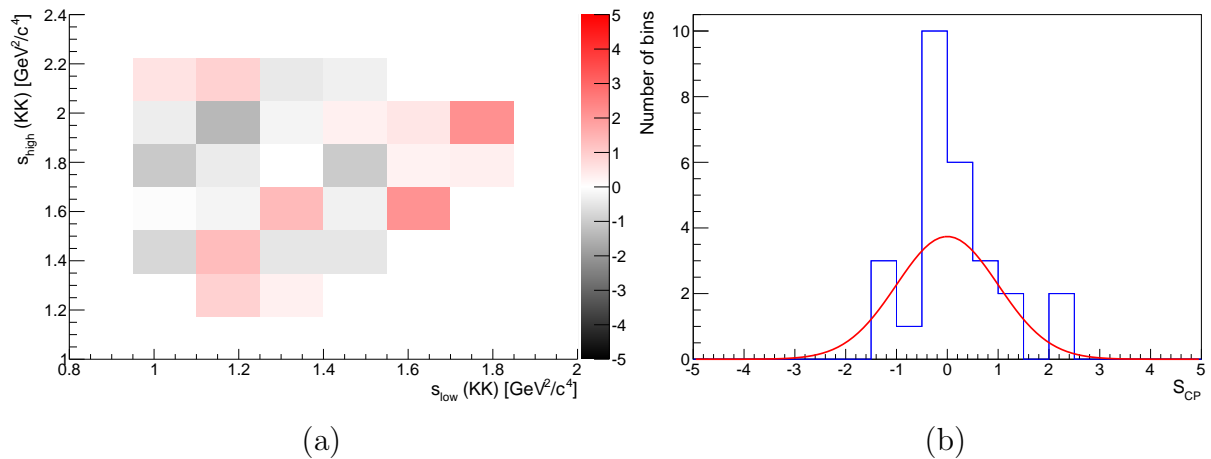


Figure 5.20: (a) Distribution of the values of S_{CP}^i with 8×8 uniform bins in the $D_s^+ \rightarrow K^- K^+ K^+$ Dalitz plot. (b) The corresponding one-dimensional distribution of S_{CP} with a standard normal Gaussian function superimposed (red-line).

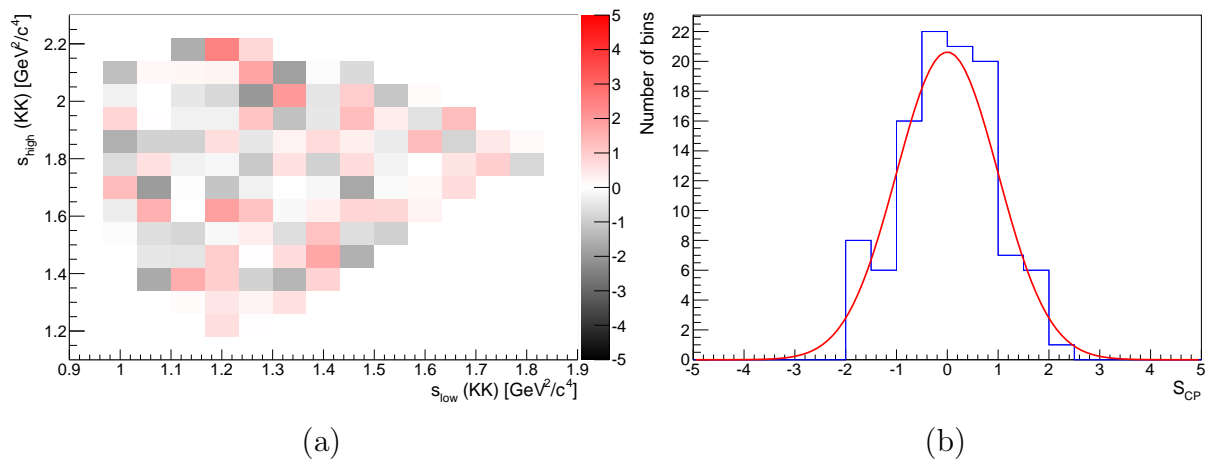


Figure 5.21: (a) Distribution of the values of S_{CP}^i with 15×15 uniform bins in the $D_s^+ \rightarrow K^- K^+ K^+$ Dalitz plot. (b) The corresponding one-dimensional distribution of S_{CP} with a standard normal Gaussian function superimposed (red-line).

Binning	N^+	N^-	α	χ^2	ndf	p-value
8×8	37,925	37,488	1.01166	21.252	26	72.8%
15×15	37,862	37,437	1.01135	91.339	106	84.4%

Table 5.7: Results for uniform binning of $D_s^+ \rightarrow K^- K^+ K^+$ Dalitz Plot in the background region.

5.5.2 Adaptive Binning

Figures 5.22, 5.23 and 5.24 show the distribution of the asymmetry variable S_{CP} for 24, 64 and 144 adaptive bins, respectively. We can observe that again the distributions follow normal Gaussian distributions. The specific results of applying the Mirandizing method in the signal region of $D_s^+ \rightarrow K^- K^+ K^+$ are summarized in Table 5.8, from which the p-values for each binning show consistency with the null CP violation hypothesis.

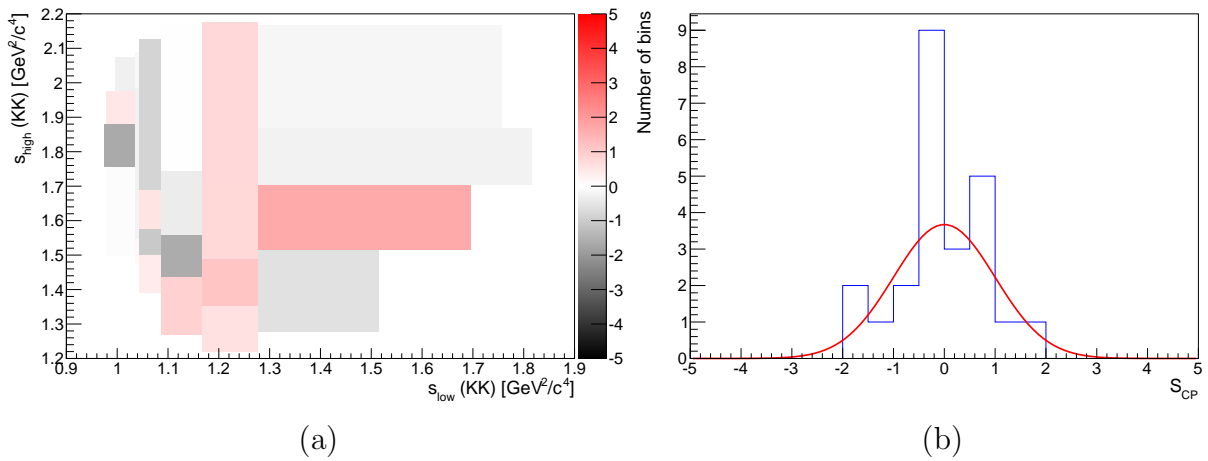


Figure 5.22: (a) Distribution of the values of S_{CP}^i with 24 adaptive bins in the $D_s^+ \rightarrow K^- K^+ K^+$ Dalitz plot. (b) The corresponding one-dimensional distribution of S_{CP} with a standard normal Gaussian function superimposed (red-line).

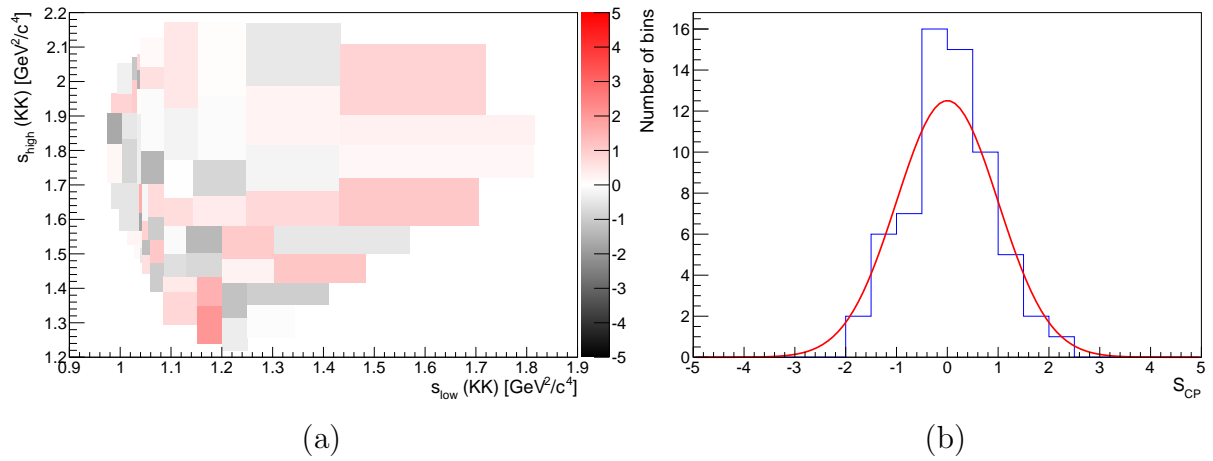


Figure 5.23: (a) Distribution of the values of S_{CP}^i with 64 adaptive bins in the $D_s^+ \rightarrow K^- K^+ K^+$ Dalitz plot. (b) The corresponding one-dimensional distribution of S_{CP} with a standard normal Gaussian function superimposed (red-line).

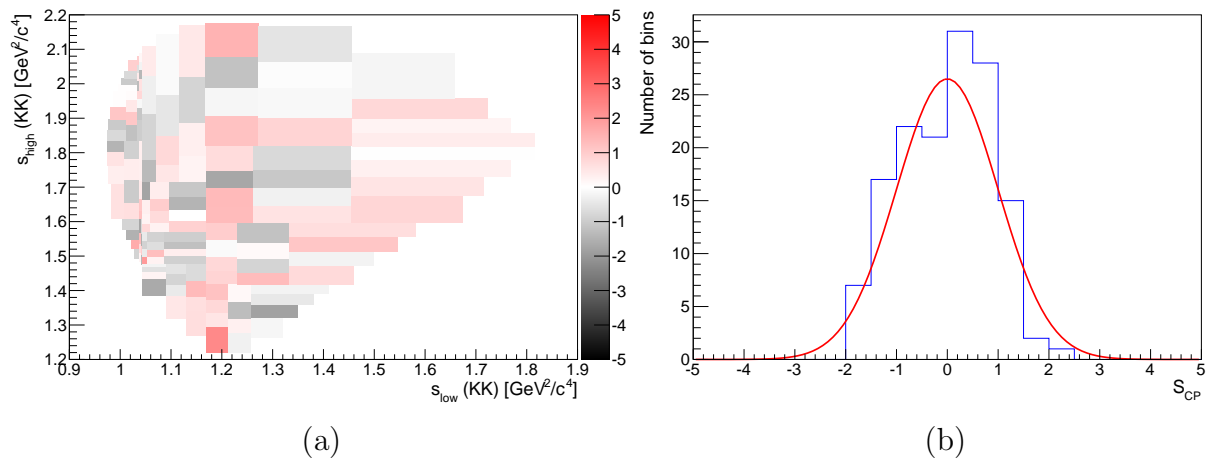


Figure 5.24: (a) Distribution of the values of S_{CP}^i with 144 adaptive bins in the $D_s^+ \rightarrow K^- K^+ K^+$ Dalitz plot. (b) The corresponding one-dimensional distribution of S_{CP} with a standard normal Gaussian function superimposed (red-line).

Binning	N^+	N^-	α	χ^2	p-value
24	37,915	37,477	1.01169	15.053	89.2%
64	37,896	37,463	1.01156	44.849	95.9%
144	37,886	37,457	1.01145	114.352	96.2%

Table 5.8: Results for adaptive binning of $D_s^+ \rightarrow K^- K^+ K^+$ Dalitz plot in the background region.

5.6

Summary of the results

We have searched for CP violation in $D_s^+ \rightarrow K^- K^+ K^+$ with a sample size of 75,413 events after checking that no nuisance asymmetries are present into the signal region of two control channels and into the sideband region of our main channel. We see no evidence for CPV in this Cabibbo-suppressed decay.

6

Conclusions and Outlook

The goal of this dissertation has been the search for CP violation through the charm decay $D_s^+ \rightarrow K^- K^+ K^+$ with data collected by the LHCb Experiment in 2012. This particular decay channel is interesting because it is a Cabibbo-suppressed decay and therefore, CP violating asymmetries are expected to be at the level of 10^{-3} , according to the Standard Model of elementary particles. Furthermore, this decay belongs to the charm-flavor sector where no CPV has ever been found.

For this purpose, we looked for local asymmetries in the Dalitz Plot for $D_s^+ \rightarrow K^- K^+ K^+$ with 75,413 events in its signal region. Our approach was based on a model-independent technique called Mirandizing method that measures the significance of this anisotropy in the phase space for D_s^+ and D_s^- through the distribution of an significance variable S_{CP} . In order to make sure that not systematic effects are introducing nuisance asymmetries, we worked with two control channels, $D^+ \rightarrow K^- \pi^+ \pi^+$ and $D_s^+ \rightarrow K^- K^+ \pi^+$, for which no CPV is expected since they are Cabibbo-favored decays. For most of them, we used just part of the full 2012 data, in particular about 181K events for the former channel and 870K events for the latter one.

We then apply the Miradizing method on the signal region of these control channels by dividing their Dalitz plots with a grid and comparing the events in corresponding bins. The distribution found for the significance variable in each channel follows a normal Gaussian distribution, ensuring that not nuisance asymmetries are present. Indeed, we performed the method by two different ways of binning the Dalitz plot. One in which all bins have the same size (uniform), and other in which all bins are equally populated (adaptive). For our main channel a further step was needed, namely to look for nuisance asymmetries that could be introduced by the background, however we conclude that this is not the case for the mass sidebands of $M(K^- K^+ K^+)$.

Finally, we studied the distribution of the significance asymmetry into the signal region of $D_s^+ \rightarrow K^- K^+ K^+$. No indication of local asymmetries are found and we conclude that with the LHCb 2012 data, there is no evidence for CP violation in this channel.

A Three-particle Decay Kinematics

This appendix describes the kinematic aspect involved in the process of a spinless particle decaying into three particles. The initial state consists, then, of a so-called mother particle (M) and the final state of three daughter particles that we are going to identify as 1,2 and 3. Indeed, the decay we are interested in would be described as

$$M \rightarrow 1 + 2 + 3$$

and the four-momenta in the Lab Frame (S) would be defined by

$$P_M = (E_M, \vec{p}_M), \quad P_1 = (E_1, \vec{p}_1), \quad P_2 = (E_2, \vec{p}_2), \quad P_3 = (E_3, \vec{p}_3), \quad (\text{A.1})$$

where E and \vec{p} are the energy and momentum of a given particle, respectively. Further, these two magnitudes are related to the mass m of the particle by the energy-momentum relation (natural units $c = 1$)

$$E^2 = p^2 + m^2. \quad (\text{A.2})$$

Since the four-momentum is conserved in every decay process, the four-momenta in (A.1) should hold the following relation

$$P_M = P_1 + P_2 + P_3. \quad (\text{A.3})$$

As each particle in the final state has three components of momentum, the system would have 9 degrees of freedom. However, the final state is constrained with the initial state by the conservation of energy and momentum, which is summarized in relation (A.3). In this way, the number of degrees of freedom is reduced to 5. Since the mother particle has no spin, the absolute orientation in space is irrelevant. Thus, the daughter particles are produced without a restricted orientation in space. This last observation can be easily understood if the system is analyzed in the Rest Frame (CM) in which the mother particle is at rest and the daughters should be produced isotropically, without a preferable orientation. Under all these conditions, only 2 degrees of freedom are needed to describe this decay process. Mathematically, the previous arguments can be described by defining the following Lorentz-invariant Dalitz variables

$$\begin{aligned} s_{12} &= (P_1 + P_2)^2 = (P_M - P_3)^2, \\ s_{23} &= (P_2 + P_3)^2 = (P_M - P_1)^2, \\ s_{13} &= (P_1 + P_3)^2 = (P_M - P_2)^2. \end{aligned} \quad (\text{A.4})$$

By summing over these new variables we get

$$\begin{aligned}
s_{12} + s_{23} + s_{13} &= \sum_{i=1}^3 (P_M - P_i)^2 = \sum_{i=1}^3 (P_M^2 + P_i^2 - 2P_M \cdot P_i) \\
s_{12} + s_{23} + s_{13} &= \sum_{i=1}^3 (m_M^2 + m_i^2 - 2P_M \cdot P_i) = 3m_M^2 + \sum_{i=1}^3 m_i^2 - 2P_M \cdot \sum_{i=1}^3 P_i \\
s_{12} + s_{23} + s_{13} &= 3m_M^2 + \sum_{i=1}^3 m_i^2 - 2P_M \cdot P_M = 3m_M^2 + \sum_{i=1}^3 m_i^2 - 2m_M^2
\end{aligned}$$

where we have used the fact that if $P = (E, \vec{p})$ is squared, $P^2 = E^2 - p^2 = m^2$ (energy-momentum relation). Finally, we get an important relation between the Dalitz variables

$$s_{12} + s_{23} + s_{13} = m_M^2 + m_1^2 + m_2^2 + m_3^2, \quad (\text{A.5})$$

which implies that only two of them are needed to describe the decay process. Therefore, each decay or event can be represented in a phase-space or plane whose axis would be two Dalitz variables, this plane is known as a Dalitz Plot (DP). From expressions (A.4), we can interpret $\sqrt{s_{ij}}$ as the invariant-mass of the subsystem containing particles i and j , that is, $\sqrt{s_{ij}} = m_{ij}$. Finally, one important feature of the Rest Frame ($\vec{p}_M = \vec{0}$) is that under this reference, the three daughters should lie in a plane. This is due to momentum conservation $\vec{p}_1 + \vec{p}_2 + \vec{p}_3 = \vec{0}$.

A.1 Kinematic Limits

Until now our analysis has been made mainly in the Lab Frame (S). However, it comes out convenient to work in a different frame (S') in which $\vec{p}_2 + \vec{p}_3 = \vec{0}$, such a frame is known as the Gottfried-Jackson Frame [44]. Consequently, into this new frame $\vec{p}'_M = \vec{p}'_1$, since momentum should also be conserved. Then, we can determine p'_1 (p'_M) from the expression for s_{23} in this frame

$$\begin{aligned}
s_{23} &= (P'_M - P'_1)^2 = (E'_M - E'_1)^2 - (\vec{p}'_M - \vec{p}'_1)^2 = E'^2_M + E'^2_1 - 2E'_M E'_1 \\
s_{23} &= m^2_M + p'^2_M + m^2_1 + p'^2_1 - 2\sqrt{(m^2_M + p'^2_M)(m^2_1 + p'^2_1)} \\
s_{23} &= m^2_M + m^2_1 + 2p'^2_1 - 2\sqrt{(m^2_M + p'^2_1)(m^2_1 + p'^2_1)}
\end{aligned}$$

$$\begin{aligned}
4(m^2_M + p'^2_1)(m^2_1 + p'^2_1) &= (m^2_M + m^2_1 - s_{23} + 2p'^2_1)^2 \\
4m^2_M m^2_1 + 4p'^4_1 + 4p'^2_1(m^2_M + m^2_1) &= (m^2_M + m^2_1 - s_{23})^2 + 4p'^4_1 + 4p'^2_1(m^2_M + m^2_1 - s_{23}) \\
4m^2_M m^2_1 &= (m^2_M + m^2_1 - s_{23})^2 - 4p'^2_1 s_{23}
\end{aligned}$$

Using the triangular function $\lambda(x, y, z) = (x + y - z)^2 - 4xy$, we get

$$p_1'^2 = \frac{\lambda(m_M^2, m_1^2, s_{23})}{4s_{23}} \quad (\text{A.6})$$

Analogously, we could also have expressed s_{23} as $(P_2' + P_3')^2$ obtaining

$$p_2'^2 = p_3'^2 = \frac{\lambda(m_2^2, m_3^2, s_{23})}{4s_{23}} \quad (\text{A.7})$$

Now we can calculate the energies of the three produced particles in frame S' from the energy-momentum relation

$$E_1'^2 = \frac{(m_M^2 + m_1^2 - s_{23})^2}{4s_{23}} + m_1^2 = \frac{(m_M^2 - m_1^2 - s_{23})^2}{4s_{23}}$$

$$E_1' = \frac{(m_M^2 - m_1^2 - s_{23})}{2\sqrt{s_{23}}} \quad (\text{A.8})$$

$$E_2' = \frac{(m_2^2 - m_3^2 + s_{23})}{2\sqrt{s_{23}}}, \quad E_3' = \frac{(m_3^2 - m_2^2 + s_{23})}{2\sqrt{s_{23}}} \quad (\text{A.9})$$

From the relations in (A.4), we can express s_{13} as

$$s_{13} = (P_1' + P_3')^2 = (E_1' + E_3')^2 - (\vec{p}_1' + \vec{p}_3')^2 = m_1^2 + m_3^2 + 2(E_1'E_3' - p_1'p_3' \cos \theta')$$

where θ' is the angle between \vec{p}_1' and \vec{p}_3' . Since we are interested in the contours or limits of the Dalitz plot, we can take the maximum and minimum of $\cos \theta'$, that is, ± 1 . Using the relations for $p_1'^2$ and $p_3'^2$, we get

$$s_{13}^{\pm} = m_1^2 + m_3^2 + \frac{1}{2s_{23}} \left[(m_M^2 - m_1^2 - s_{23})(m_3^2 - m_2^2 + s_{23}) \pm \lambda^{1/2}(m_M^2, m_1^2, s_{23})\lambda^{1/2}(m_2^2, m_3^2, s_{23}) \right] \quad (\text{A.10})$$

as the contours of a Dalitz plot described in terms of s_{12} and s_{23} as its axis.

In order to get the other limits for the Dalitz plot, we are going back to the Rest Frame (CM). The maximum value of, for example, s_{12} would occur when the third particle gets its minimum energy, that is, m_3 in natural units. Then, the energy available for the subsystem m_{12} would be $(M - m_3)$ which means that $s_{12,max} = (M - m_3)^2$. On the other side, the minimum value of s_{12} would occur when the only energy available for this subsystem is just enough to create it, that is, $s_{12,min} = (m_1 + m_2)^2$. Analogously,

$$s_{23,max} = (m_2 - m_3)^2, \quad s_{23,min} = (m_2 + m_3)^2.$$

Figure A.1 shows a typical Dalitz Plot whose axis are s_{12} and s_{23} .

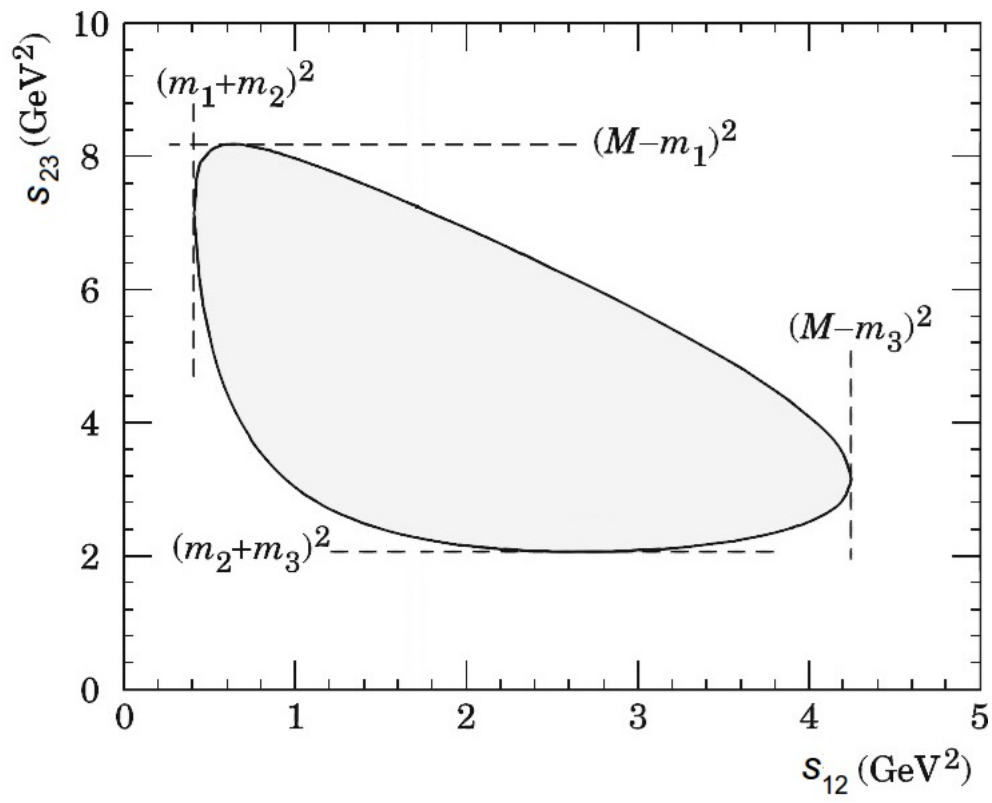


Figure A.1: Dalitz Plot for a three-particle decay including its kinematic limits.

B Definition of Variables for Data Selection

The relevant variables for an event to be considered a good candidate include the kinematic variables of the particles involved in a decay such as momentum (p), transverse momentum (p_T) and energy (E_T). The Particle Identification (PID) variables are based on the information provided by RICH detectors, muon system, and calorimeters. To distinguish between pions and kaons the $dllk\pi$ variable is used, defined as the difference of logarithm of the likelihoods between the kaon and pion mass hypotheses, $\ln(LL_K) - \ln(LL_\pi)$. The characteristics of some of the variables used in accordance to the decay's topology, shown in Figure B.1, are described

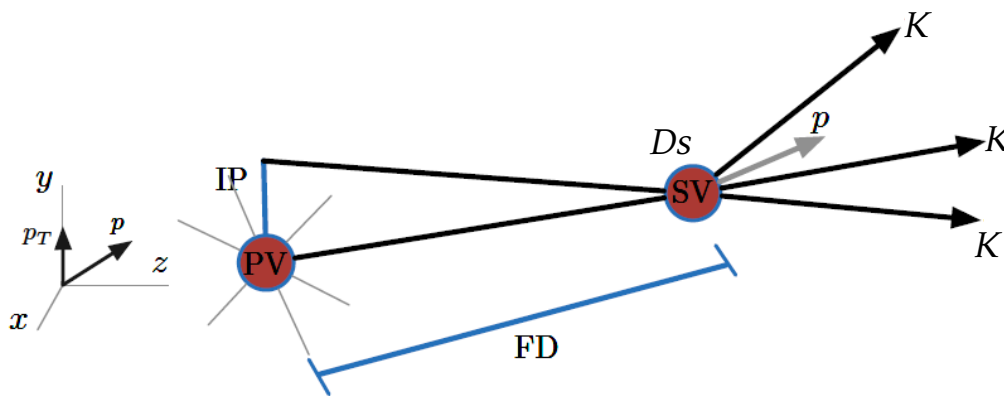


Figure B.1: Production process of the meson D_s^+ decaying in $K^-K^+K^+$.

D_MM *Invariant mass of the D_s^+ candidate.*

It is obtained from information of the 4-momenta of each daughter particle. Its value is required to be close to the nominal mass of D_s^+ .

D_PT *Transverse moment of D_s candidate.* Measured from the D_s meson in the perpendicular direction with z -beam axis-, requiring P_T above a certain value, being the D_s meson a heavy particle.

PV Primary Vertex (PV)

Point in which the $p - p$ interaction occurs and where a large portion of D 's is produced.

SV Secondary Vertex (SV)

Decay point of D_s meson in its products, obtained from the track intersection of the three daughter particles.

D_FD_CHI2_OWNPV Flight distance related to the its own primary vertex.

Distance between PV and SV, in other words, the distance between the collision point (where D_s is created) and the decay point. Information about its value is provided by VELO.

IP Impact Parameter.

Shortest distance between a reconstructed track and the primary vertex. It can be applied to the D_s or to their daughters. For these, it is required that they are not originating from the primary vertex, i.e. their IP χ^2 must be greater than a given value. χ^2 distribution tells us the extent to which the observed values deviate from the expected value.

pi_IPCHI2_OWNPV ($i = 1, 2, 3$) χ^2 of the daughters IP with reference to its own Primary Vertex.

DIRA Cosine of the angle between the flight direction and the reconstructed moment of D_s meson from the three daughters. For real three body D_s decays, must be close to 1.

pi_PT ($i = 1, 2, 3$) Transverse moment of the daughters.

As the D_s meson is a particle produced with large transverse momentum, this becomes an important discriminant of noise in daughters. However, the low $p - T$ region is located on the edges of the Dalitz plot, which could imply that by implementing a strong cut in any of these variables, undesirable effects on the final graph might be introduced.

DOCA_ij Distance of minimum approach between the tracks i and j .

Given two tracks, the minimum distance between them is calculated.

DII_{K π} Particle Identification

From the quality of identification of the daughter particles it depends the confidence in the D_s meson candidates selection. In our case we need to identify in the best possible way pions and kaons. Initially at the RICH

system, each track it is associated to a probability to be originated by one of the five possible particles in the interaction such as pions, kaons, protons, electrons or muons. The likelihood hypothesis of the particles is used and in other to better observe the changes in values, we calculate the logarithmic difference of these amounts. For instance, for the $K\pi$ separation the expression $\ln\mathcal{L}(K) - \ln\mathcal{L}(\pi) = DLL(K - \pi)$ is obtained, and we choose the value that is closest to our requirement.

χ^2/ndof χ^2 value of the track reconstruction fit.

This adjustment is applied in the reconstruction of good candidates for daughters, χ^2/ndof is also used in the selection of stripping to improve the sample's quality.

PTsum Scalar p_T sum of the three kaons.

As D_s is a particle with high PT, the produced particles will also have elevated PT values. PTsum is defined as the scalar sum of the three daughters PTs and it is required to be greater than a certain value.

Variable	Cuts
Track χ^2	< 3
p_T	$> 250 \text{ MeV}/c^2$
p	$> 200 \text{ MeV}/c^2$
IP χ^2	> 4
PIDK	> 7
DOCA χ^2	< 50
Highest IP χ^2	> 10
DOCA max	$< 0.5 \text{ mm}$
p_T Sum	> 2800
DPT	> 1000
dVx χ^2	< 30
DIP χ^2	< 12
Number of tracks	< 500
FD χ^2	> 125
Mass	1800-2040

Table B.1: Stripping20: Off-line selection criteria for the LHCb data in Run I (2012) for candidates of $D_s^+ \rightarrow K^- K^+ K^+$.

Bibliography

- [1] CANETTI, L.; DREWES, M.; SHAPOSHNIKOV, M. *Matter and antimatter in the universe*. New J. Phys. 14 (9), 095012, 2012. 1
- [2] PERKINS, D. H. *Introduction to High Energy Physics*. Cambridge University Press, 2000. 1
- [3] CHRISTENSON, J. H.; CRONIN, J. W.; FITCH, V. L.; TURLAY, R. *Evidence for the 2π Decay of the K_0^2 Meson*. Physical Review Letters, 13 1381, 2.3.3, 2.4, 1964.
- [4] NA48 COLLABORATION. *A new measurement of direct CP violation in two pion decays of the neutral kaon*. Physics Letters B. 465, 1999, 335-348 p. 1, 2.4
- [5] AUBERT, B. et al. (BABAR COLLABORATION). *Measurement of CP-Violating Asymmetries in B_0 Decays to CP Eigenstates*. Phys. Rev. Lett. 86, 2515 – Published 19 March 2001. 1
- [6] ABE, K. et al. (BELLE COLLABORATION). *Observation of Large CP Violation in the Neutral B Meson System*. Phys. Rev. Lett. 87, 091802 – Published 14 August 2001. 1
- [7] CRUZ, M. *Medida da razão de ramificação do canal $D_s^+ \rightarrow \pi^- K^+ K^+$ relativa ao canal $D_s^+ \rightarrow K^- K^+ \pi^+$ no Experimento LHCb*. MSc Thesis, PUC-Rio, 2014. 2.1
- [8] ABE, F. et al. (CDF COLLABORATION). *Observation of Top Quark Production in $\bar{p}p$ Collisions with the Collider Detector at Fermilab*. Phys. Rev. Lett. 74, 2626 – Published 3 April 1995. 2.1
- [9] ABACHI, S. et al. (D0 COLLABORATION). *Search for High Mass Top Quark Production in $\bar{p}p$ Collisions at $\sqrt{s} = 1.8$ TeV*. Phys. Rev. Lett. 74, 2422 – Published 27 March 1995. 2.1
- [10] DONUT COLLABORATION. *Observation of tau neutrino interactions*. Physics Letters B, Volume 504, Issue 3, 12 April 2001, 218–224 p. 2.1
- [11] CMS COLLABORATION. *Observation of a new boson at a mass of 125 GeV with the CMS experiment at the LHC*. Physics Letters B, 716, 2012, 30-61 p. 2.1

- [12] ATLAS COLLABORATION. *Observation of a new particle in the search for the Standard Model Higgs boson with the ATLAS detector at the LHC*. Physics Letters B, **716**, 2012, 1-29 p. 2.1
- [13] LHCb COLLABORATION. *Observation of the resonant character of the $Z(4430)^-$ state*. arXiv:1404.1903v1 [hep-ex] 7 April 2014. 1
- [14] AAIJ, R. et al. *Observation of $J/\psi p$ Resonances Consistent with Pentaquark States in $\Delta 0_b \rightarrow J/\psi K^- p$ Decays*. Physical Review Letters, PRL **115**, 072001, 2015. 1
- [15] GLASHOW, S. L.; ILIOPOULOS, J.; MAIANI, L. *Weak Interactions with Lepton-Hadron Symmetry*. Physical Review D, **2** (7), 1970, 1285-1292 p. 2.3.1
- [16] BOWLER, M. G. *Femtophysics, A Short Course on Particle Physics*. Pergamon Press, 1990. 2.3.1
- [17] HALZEN, F.; MARTIN, A. D. *Quarks and Leptons: An Introductory Course in Modern Particle Physics*. John Wiley & Sons, 1984. 2.3.3
- [18] LEE, T. D.; YANG, C. N. *Question of Parity Conservation in Weak Interactions*. Physical Review, **104** 1, 1956. 2.3.3
- [19] WU, C. S.; AMBLER, E.; HAYWARD, R. W.; HOPPES, D. D.; HUDSON, R. P. *Experimental Test of Parity Conservation in Beta Decay*. Physical Review, **105** 1413, 1957. 2.3.3
- [20] COUTINHO, R. S. *Estudo do decaimento $B^\pm \rightarrow K^\pm \pi^\pm \pi^\mp$ no experimento LHCb*. MSc Thesis, PUC-Rio, 2011. 2.4
- [21] SAKHAROV, A. D. *Violation of CP invariance, C asymmetry, and baryon asymmetry of the universe*. Journal of Experimental and Theoretical Physics. Vol. 5, 1967. 24-27 p. 2.4
- [22] GORDON, H. *Searches for CP Violation in Charmed Meson Decays. A Study of $D^+ \rightarrow K^- K^+ \pi^+$ at the LHCb Experiment*. Springer International Publishing Switzerland, 2014. 2.5
- [23] OLIVE, K. A. et al. (Particle Data Group). Chin. Phys. C. 38(9):09001, 2014. 2.6
- [24] CAHN, R. N.; GOLDHABER, G. *The Experimental Foundations of Particle Physics*. Cambridge University Press, 2009. 3.1

- [25] DAS, A.; FERBEL, T. *Introduction to Nuclear and Particle Physics*. World Scientific, 2003. 3.1
- [26] EVANS, L. (Editor). *The Large Hadron Collider: A Marvel of Technology*. EPFL Press, 2009. 3.2
- [27] DE AQUINO, P. *Beyond Standard Model Phenomenology at the LHC*. Switzerland. Springer, 2014. 3.2
- [28] LHCb COLLABORATION. *LHCb VELO Upgrade Technical Design Report*. CERN/LHCC, 2013-021, LHCb TDR 13, 2013. 3.3.1
- [29] LHCb COLLABORATION. *Performance of the LHCb Vertex Locator*. CERN/LHCC, CERN-LHCb-DP-2014-001, arXiv:1405.7808v2, 2014. 3.3.1
- [30] LHCb COLLABORATION. *Reoptimized Detector Design and Performance*. CERN/LHCC 2003-030, LHCb TDR 9, 2003. 3.3.1
- [31] LHCb COLLABORATION. *LHCb RICH Technical Design Report*. CERN LHCC LHCb TDR 3, 2000-037, 2000, 1-9 and 47-56 p. 3.3.1, 3.3.3
- [32] LHCb COLLABORATION. *LHCb Inner Tracker Technical Design Report*. CERN/LHCC 2002-029, LHCb TDR 008, 2002. 3.3.1
- [33] LHCb COLLABORATION. *LHCb Outer Tracker Technical Design Report*. CERN/LHCC/2001-024, LHCb TDR 006, 2001, 1-9 p. 3.3.1
- [34] ADEVA, B. *The silicon tracker of the LHCb Experiment*. Nuclear Science Symposium Conference Record, 2004 IEEE. 2, 2004, 1179-1182 p. 3.3.1
- [35] LHCb COLLABORATION. *LHCb Magnet: Technical Design Report*. CERN/LHCC, LHCb-TDR-1, 2000. 3.3.1
- [36] HUTCHCROFT, D. *VELO Pattern Recognition*. LHCb-VELO, 2007-013, 2007, 1-5 p. 3.3.2
- [37] LHCb COLLABORATION. *LHCb Calorimeters Technical Design Report*. CERN/LHCC, 2000-0036, LHCb TDR 2, 2000. 3.3.3
- [38] LHCb COLLABORATION. *LHCb Muon System Technical Design Report*. LHCb-VELO 2007-013, 2001-010, LHCb TDR 4, 2001. 3.3.3
- [39] LAMONT, M. *Status of the LHC*. Journal of Physics: Conference Series. Vol. 455-012001, 2013. doi:10.1088/1742-6596/455/1/012001. 4

- [40] MOLINA, J. *Busca de violação de CP em decaimentos charmosos hadrônicos em três corpos*. MSc Thesis, PUC-Rio, 2011. 4.2
- [41] BEDIAGA, I.; BIGI, I. I.; GOMES, A.; GUERRER, G.; MIRANDA, J.; DOS REIS, A. C. *On a CP anisotropy measurement in the Dalitz plot*. Physical Review D, **80**, 096006, 2009. 5
- [42] LHCb COLLABORATION. *Search for CP Violation in the decay $D^+ \rightarrow \pi^- \pi^+ \pi^+$* . Physics Letters B, **728**, 2014, 585-595 p. 5.1
- [43] LYONS, L. *Statistics for Nuclear and Particle Physicists*. Cambridge University Press, 1986. 5.1
- [44] SALGADO, C.W.; WEYGAND, D. P. *On the Partial-Wave Analysis of Mesonic Resonances Decaying to Multiparticle Final States Produced by Polarized Photons*. arXiv:1310.7498v2 [nucl-ex]. 16 December 2013. A.1